Review

Ultrathin structured photocatalysts: A versatile platform for CO_2 reduction

Jun Xiong[a,c,1], Pin Song[b,1], Jun Di[b,*], Huaming Li[a,*]

[a] Institute for Energy Research, Jiangsu University, 301 Xuefu Road, Zhenjiang, 212013, PR China
[b] Center for Programmable Materials, School of Materials Science & Engineering, Nanyang Technological University, Singapore, 639798, Singapore
[c] School of Mechanical and Aerospace Engineering, Nanyang Technological University, Singapore, 639798, Singapore

ARTICLE INFO

ABSTRACT

Sustainable photocatalytic CO_2 reduction to produce valuable hydrocarbon fuels is an attractive pathway to mitigate current energy issue and greenhouse effect of CO_2. Due to the unique structures and unusual physicochemical properties, ultrathin structured materials display promising opportunities to achieve efficient CO_2 photoreduction performance. In this review, the state-of-the-art progress on ultrathin structured photocatalysts for CO_2 photoreduction is reviewed. We start with the basic understanding on CO_2 photoreduction and several points worthy of notice in CO_2 photoreduction. Then advancements of diversified ultrathin photocatalysts towards CO_2 photoreduction classified as 1D nanotubes/wires/rods/ribbons, 2D nanosheets/plates, and 3D architectures assembled with ultrathin structures are presented. Various strategies to further tailor the performance of CO_2 reduction are discussed with the emphasis of structure-activity relationship, such as atomic incorporation, vacancy engineering, crystal facet tailoring, surface modification and heterostructure construction. Finally, the future opportunities and challenges for development of ultrathin structured photocatalysts for CO_2 reduction are presented.

1. Introduction

Excessive combustion of fossil fuel with largely effluent CO_2 has cause global warming issue. Converting CO_2 molecule to value-added carbon products via sustainable solar energy has been considered as an attractive route to address current energy issue and mitigate the greenhouse effect of CO_2 [1–4]. Under the irradiation, CO_2 molecules can be ideal reduced over suitable photocatalysts and H_2O assistance, with the main products such as CO, HCHO, HCOOH, CH_3OH, CH_4, C_2H_5OH, according to diverse transferred electron numbers [5,6]. However, CO_2 molecule is terrific thermodynamic stable with the dissociation energy of C=O bond is higher than $750\,kJ\,mol^{-1}$, which greatly limit the catalytic transformation efficiency over voluminous photocatalysts.

It has been widely accepted that during the photocatalytic reaction processes, three crucial factors essentially determine the catalytic efficiency, namely light harvesting, charge separation and transportation as well as surface catalysis reactions [7–9]. To build desired photocatalysts towards CO_2 reduction, several requirement should be satisfied from above mentioned aspects. Firstly, the robust light harvesting ability is needed to provide sufficient electron-hole pairs. Secondly, the produced electron-hole pairs should be effective

separated and the electrons should transfer easily from the inside of materials to the surface. Thirdly, the surface structure of photocatalysts should be favorable for CO_2 molecule adsorption and activation as well as the conduction band (CB) potential should meet the thermodynamic requirement for CO_2 reduction. Fourthly, the formed carbon-based products should be desorbed from the surface easily to accelerate the reaction and the photogenerated holes can be consumed by oxidation of water to yield O_2 (non-ideal condition using sacrificial reagents to consume holes) [10]. Up to now, although numerous photocatalysts have been reported for CO_2 reduction [11–15], most of them are subjected to low transformation efficiency, poor selectivity, instability and suffer from H_2 evolution side reaction from H_2O.

Recent studies found that ultrathin structured photocatalysts (such as ultrathin nanosheets, nanotubes, nanowires) shows enormous advantages towards CO_2 photoreduction due to the unique structure features [16,17]. After the thickness of bulk materials reduced to atomic-level ultrathin, the specific surface area can be drastic increased, strong quantum confinement effect and surface effects are available [18]. Through the tuning of thickness, the band structures of semiconductors can be adjusted. Generally, the band gap will be broaden with the upshift of conduction band and downshift of valence band due to the well-known quantum confinement effect. Moreover, the ultrathin

---

thickness can enable the photogenerated charge carriers fast migrate from the materials inside to the surface, reducing the recombination rate during migration. At the same time, the abundant surface atoms with dangling bonds can not only build interaction with CO_2 molecule, but also favors the formation of surface def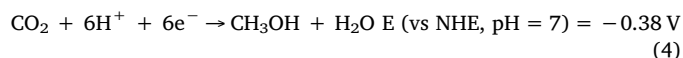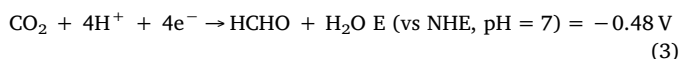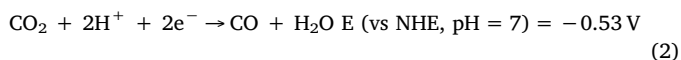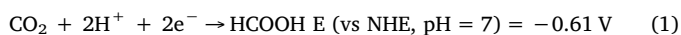ects for better CO_2 activation and conversion [19]. Benefiting from these advantages, the ultrathin structured photocatalysts show tremendous prospect for CO_2 photo-reduction, thus it is highly desirable to give an inspiring review in this domain to guide the further developments.

In this review, it will first present an introduction of basic understanding on CO_2 photoreduction and some matters need attention. Then, various ultrathin structured photocatalysts will be summarized to demonstrate the advantages and advancements for CO_2 reduction. Then effective strategies commonly employed to tune the surface coordination structure, electronic structure, carrier concentration and charge separation for boosting the CO_2 photoreduction performance have been summarized. The authors hope that this review will encourage wider research towards ultrathin structured photocatalysts for CO_2 reduction.

2. Basic understanding on CO_2 photoreduction

CO_2 is an inert chemical specie in the nature since the high dissociation energy of C=O bond (750 kJ mol^{-1}), and a large highest occupied molecular orbital-lowest unoccupied molecular orbital (HOMO–LUMO) energy gap (13.7 eV) [20]. Compared with Gibbs free energy change of H_2O spitting (237.2 kJ mol^{-1}), converting CO_2 and H_2O into hydrocarbon fuels require much larger positive change of Gibbs free energy, make this process more challenge. For instance, CO_2 reduction to yield CH_3OH and CH_4 is an uphill reaction with 702.2 and 818.3 kJ mol^{-1} change of Gibbs free energy, respectively [21]. A distinguished mechanism for CO_2 reduction is the single-electron transfer activation to the adsorbed CO_2 at active sites to form $CO_2^{\cdot-}$ intermediate. However, this process is thermodynamic unfavorable with very negative equilibrium potential of -1.9 V versus NHE is required, due to the high LUMO level of CO_2 [22]. The large reorganizational energy from the linear structure of CO_2 to the bending structured $CO_2^{\cdot-}$ radical anion make this single-electron activation process to be the rate-determining step for CO_2 photoreduction [21]. To overcome this issue, one of the effective approach is tune the surface atomic structure of catalysts to form favorable sites such as Ti^{3+} sites on TiO_2 and surface oxygen vacancies [2]. For example, one oxygen atom of the CO_2 will prefer to be adsorbed at oxygen vacancy via bridging structure. The electron-rich surface electron centers of oxygen vacancy can lower the energy barrier for one-electron transfer to CO_2 and will facilitate the formation of negatively charged $CO_2^{\cdot-}$ intermediate.

Another route is bypass the single-electron activation of forming $CO_2^{\cdot-}$ radical via multiple proton-coupled electron transfer approach [23]. As shown below, on the basis of the transferred electron and proton numbers, different products can be yielded, such as HCOOH, CO, HCHO, CH_3OH, CH_4, C_2H_5OH, C_2H_6, and so on (Eqs. (1)–(7)). However, the multiple proton-coupled electron transfer process require sufficient available photogenerated electrons and protons. The formation of CH_4 need eight electrons and eight protons involved reduction, let alone the multi-carbon products. This large kinetic barrier limits the productivity and selectivity. In comparison, this reduction process is prefer to form CO and HCOOH via two-electron reaction. Moreover, the two-electron competing reaction of H_2 evolution from H_2O reduction will simultaneously take place (Eq (8)), further lowering the reaction selectivity [24].

$$CO_2 + 2H^+ + 2e^- \rightarrow HCOOH \quad E \text{ (vs NHE, pH = 7)} = -0.61 \text{ V} \quad (1)$$

$$CO_2 + 2H^+ + 2e^- \rightarrow CO + H_2O \quad E \text{ (vs NHE, pH = 7)} = -0.53 \text{ V} \quad (2)$$

$$CO_2 + 4H^+ + 4e^- \rightarrow HCHO + H_2O \quad E \text{ (vs NHE, pH = 7)} = -0.48 \text{ V} \quad (3)$$

$$CO_2 + 6H^+ + 6e^- \rightarrow CH_3OH + H_2O \quad E \text{ (vs NHE, pH = 7)} = -0.38 \text{ V} \quad (4)$$

$$CO_2 + 8H^+ + 8e^- \rightarrow CH_4 + 2H_2O \quad E \text{ (vs NHE, pH = 7)} = -0.24 \text{ V} \quad (5)$$

$$2CO_2 + 12H^+ + 12e^- \rightarrow C_2H_5OH + 3H_2O \quad E \text{ (vs NHE, pH = 7)} = -0.33 \text{ V} \quad (6)$$

$$2CO_2 + 14H^+ + 14e^- \rightarrow C_2H_6 + 4H_2O \quad E \text{ (vs NHE, pH = 7)} = -0.27 \text{ V} \quad (7)$$

$$2H_2O + 2e^- \rightarrow 2OH^- + H_2 \quad E \text{ (vs NHE, pH = 7)} = -0.41 \text{ V} \quad (8)$$
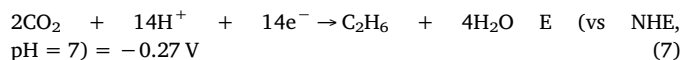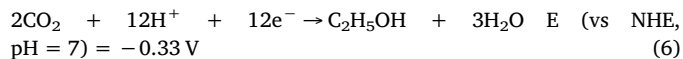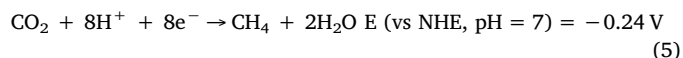
During the CO_2 photoreduction evaluation process, several factors should be taken into consideration. Firstly, the pH value of solution is usually close neutral since the alkaline condition easy to convert CO_2 into CO_3^{2-} or HCO_3^-, while acid solution favors H_2 evolution. Secondly, H_2O is regarded as ideal proton source for CO_2 photoreduction [25]. The oxidation half-reaction for the generation of oxygen gas should be checked. Take the $2CO_2 \rightarrow 2CO + O_2$ process for example, the ideal stoichiometric ratio 2:1 of $CO:O_2$ should be observed. In some systems, the sacrificial agent such as triethanolamine (TEOA), ascorbic acid is usually used for the consumption of holes. It should be carefully for the production rate evaluation since the carbon-based products and H_2 may also come from these oxidative cycles [26]. Thirdly, isotope labeling experiments using $^{13}CO_2$ molecules should ideally be performed to ensure the actual carbon source is CO_2 [27]. The corresponding ^{13}C products should be well observed via gas chromatography-mass spectrometry (GC–MS) and without ^{12}C related products. Fourthly, generally, the performance evaluation of CO_2 reduction efficiency is use rate of production evolution, such as with a unit of μmol g^{-1} h^{-1}. Since the experimental conditions employed for various systems are rather different, such as catalysts dosage, light source, reaction type (liquid-solid or gas-solid), the directly comparison of activities via evolution rate is inadvisable. Thus, it is desirable to measure the apparent quantum yield (AQY) of the reduction reaction, with the eqn 100% $\times (\Sigma_i n_i m_i)$/number of incident photons. The n_i and m_i represent the required electron number for the formed diverse products and the molecular amount of formed products, respectively. Fifthly, since the formation of multifarious products require different reduction potentials, the selectivity of both gaseous products and liquid products should be well determined. Considering the product separation is quite a complex process, it is desirable to build reaction systems with highly selectivity. Moreover, the stability of photocatalysts should be well explored due to the potential industrial application. Generally, the dominating reported photocatalysts can only maintain the activity from several hours to several days. Longer time measurements should be performed or the intrinsic reason exploration of photocatalysts structural changes should be conducted for the inactivation. Sixthly, the CO_2 molecule can serve as an electron acceptor and donor simultaneously to form diverse coordination on the materials surface, owing to the C atom can work as Lewis acid to gain electrons and O atom can act as Lewis base to donate electrons. Single or two atom coordination of CO_2 with single or two surface atom in catalysts are all feasible. Different bounding mode will affect the formation of diverse intermediates and reaction steps and thus determine the final products. Therefore, it is desirable to explore the adsorption and activation modes of CO_2 molecule on the specific photocatalysts. Advanced in situ characterization techniques such as in situ Fourier transform infrared spectroscopy (FT-IR), in situ X-ray absorption fine structure (XAFS) should be employed to explore the intermediates during CO_2 photoreduction.

3. Diversified ultrathin structured photocatalysts

Various ultrathin structured photocatalysts have been developed towards CO_2 reduction such as 1D nanotubes/wires/rods/ribbons, 2D
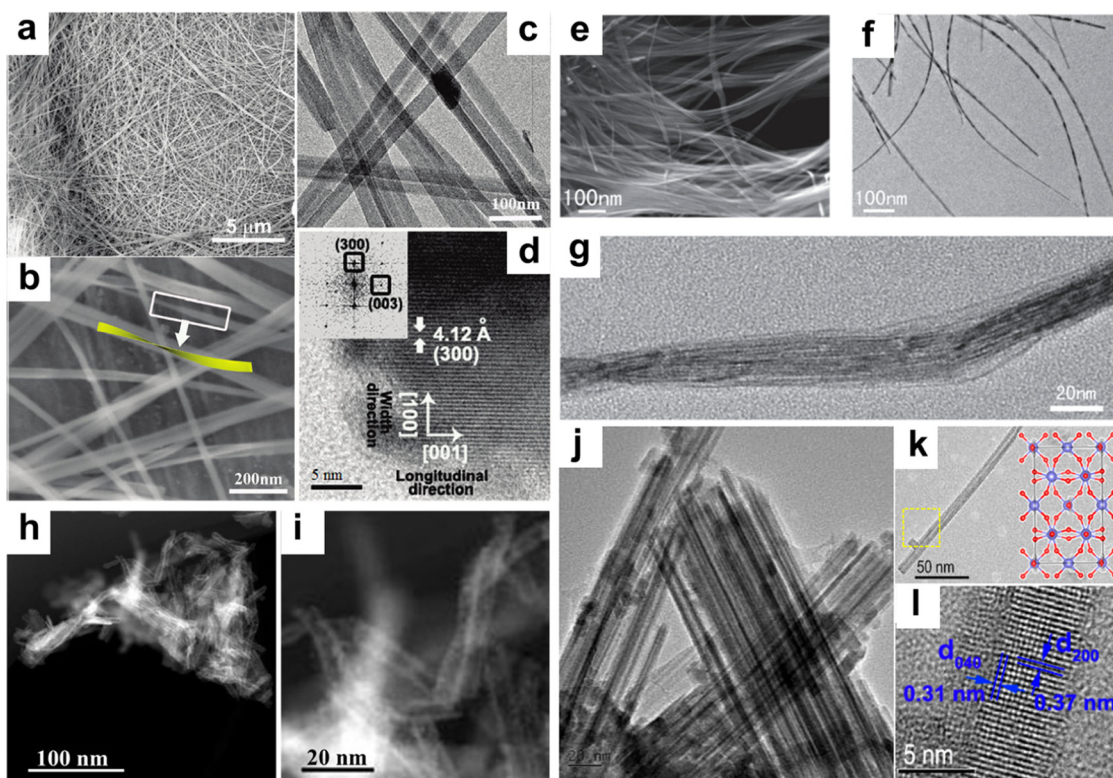
Fig. 1. (a, b) SEM, (c) TEM, and (d) HRTEM images of Zn_2GeO_4 nanoribbons, (e, f, g) SEM, TEM, and HRTEM images of the $W_{18}O_{49}$ nanowires, (h, i) aberration-corrected HAADF-STEM images of $Bi_{12}O_{17}Cl_2$ nanotubes, (j, k, l) TEM, HRTEM images of $WO_3 \cdot 0.33H_2O$ nanotubes, reproduced with permission from ref. [28] and [37], American Chemical Society and ref. [29] and [30], Wiley-VCH.

nanosheets/plates, and 3D architectures assembled with ultrathin structures. The dominating synthetic method for these ultrathin structures concentrated on solvothermal method, surfactant self-assembly, liquid exfoliation, template-directed method and inorganic-organic lamellar hybrid intermediate strategy.

3.1. 1D ultrathin structure

As early as ten years ago, Zn_2GeO_4 ultralong and ultrathin nanoribbons has been developed by Zou's et al. for CO_2 photoreduction [28]. Through a solvothermal process with ethylenediamine/water solvent, the thickness of Zn_2GeO_4 nanoribbons can be controlled to 7 nm, about five repeating cell units (Fig. 1a–d). In the gas-solid system, the Zn_2GeO_4 nanoribbons demonstrates the ability to convert CO_2 to CH_4 under light irradiation. However, the Zn_2GeO_4 nanoribbons can only respond to ultraviolet light and displays low CH_4 generation rate about $0.4 \mu mol\, g^{-1}\, h^{-1}$ during 15 h. After the addition of cocatalyst of 1 wt % Pt and 1 wt % RuO_2, the rate can be improved to about $6.3 \mu mol\, g^{-1}\, h^{-1}$. Soon afterwards, many 1D ultrathin structured materials have been explored for CO_2 photoreduction. Ye's et al. prepared ultrathin $W_{18}O_{49}$ nanowires with diameters below 1 nm (Fig. 1e–g) [29]. The ultrathin $W_{18}O_{49}$ nanowires can deliver a CO_2 reduction performance for CH_4 generation rate of $666\, ppm\; g^{-1}\, h^{-1}$ ($11.31 \mu mol\, g^{-1}\, h^{-1}$) under visible light. Under full-arc xenon lamp irradiation, the production rate of CH_4 can be further increased to $50,000\, ppm\; g^{-1}\, h^{-1}$ ($858 \mu mol\, g^{-1}\, h^{-1}$). Apart from nanoribbons and nanowires, nanotubes can also display outstanding performance for photocatalytic CO_2 reduction. For example, our group prepared $Bi_{12}O_{17}Cl_2$ superfine nanotubes with bilayer thickness of the tube wall via polyvinyl pyrrolidone (PVP) assisted solvothermal process (Fig. 1h, i) [30]. Benefiting from the surface structural distortion to create oxygen vacancies and ultrathin tubular structure to directionally separate charges, the as-prepared $Bi_{12}O_{17}Cl_2$ nanotubes can display a

16.8 times higher activity than that of bulk $Bi_{12}O_{17}Cl_2$ for CO generation in pure water, reaching $48.6 \mu mol\, g^{-1}\, h^{-1}$. The AQY of $Bi_{12}O_{17}Cl_2$ nanotubes is calculated to be 0.14% at 400 nm. ^{13}C isotope labeling experiment confirm the CO is indeed derive from the used CO_2. To insight the photoreduction process of CO_2 over $Bi_{12}O_{17}Cl_2$ nanotubes, in situ Fourier transform infrared spectroscopy (FTIR) is employed. The gradually increased signal at $1565\, cm^{-1}$ is ascribed to COOH* intermediate, revealing the activation and reaction of adsorbed CO_2. At the same time, the unique ultrathin tubular structure enable the higher adsorption amount of CO_2 and better CO liberation, contribute to the excellent photoreduction performance.

There are several other systems for the formation of CH_4 and CO via CO_2 photoreduction, such as C,N doped sodium titanate nanotubes [31], TiO_2 nanotubes [32], Mo-doped $WO_3 \cdot 0.33H_2O$ nanorods [33], $Na_2V_6O_{16} \cdot xH_2O$ nanoribbons [34], and $In_2Ge_2O_7(En)$ nanowires [35]. The Bi_2S_3 nanoribbons is found to be able to convert CO_2 into methanol with an optimized performance of $32 \mu mol\, g^{-1}\, h^{-1}$ under visible light [36]. In addition to the single-carbon products, the multi-carbon products can also be produced over 1D ultrathin structure. Ishihara et al. demonstrated the ultrathin $WO_3 \cdot 0.33H_2O$ nanotubes can realize CO_2 photoreduction to CH_3COOH in pure water (Fig. 1j–l) [37]. Under solar light, the $WO_3 \cdot 0.33H_2O$ nanotubes can deliver an average productivity of about $9.4 \mu mol\, g^{-1}\, h^{-1}$ for CH_3COOH, with a high selectivity of 85%. Study found that the collaboration of surface V_o and hydroxyl groups are regarded as the main reactive sites for the high selectivity and the reaction pathway is $CO_2 \rightarrow {}^*COOH \rightarrow (COOH)_2 \rightarrow CH_3COOH$. ^{13}C-labeled experiment also prove the produced CH_3COOH is come from CO_2 photoreduction. It is notable that no O_2 can be produced during the photoreaction process. Instead, the photogenerated holes oxidized the H_2O to yield H_2O_2, with $17.6 \mu mol\, H_2O_2$ can be detected after 10 h reaction. In situ FTIR exploration demonstrate a reaction to generate the COOH intermediate via the surface bicarbonate species and hydroxyl, which is kinetically dominant critical intermediate

leading to CO_2 reduction. Despite these advancements, the studies regarding 1D ultrathin structure for CO_2 photoreduction is still at its infancy stage. More substantial explorations are desired to further boost the CO_2 photoreduction performance.

3.2. 2D ultrathin structure

2D ultrathin nanosheets are considered as the most widely studied architecture for photocatalysis due to the hot research of 2D materials. Due to the unique structure and physicochemical property, diverse 2D ultrathin nanosheets have been developed towards CO_2 photoreduction, such as TiO_2, WO_3, Co_3O_4, C_3N_4, CuS, SnS_2, $Co_{0.85}Se$, $ZnIn_2S_4$, $SrNb_2O_6$, ZnAl LDH, BiOBr, $Bi_4O_5Br_2$, BiOI, Bi_2WO_6, Bi_2MoO_6, $BiVO_4$, Zn-MOF, SAPO-5 and so on [38–56].

Ultrathin TiO_2 flakes with controlled thickness of 1.66 nm is demonstrated for CO_2 photoreduction to yield formate [38]. The ultrathin structure endows the TiO_2 flakes with ultrahigh fraction of surface atoms towards CO_2 reduction and create higher density of states near Fermi level with increased conductivity. As a consequence, the ultrathin TiO_2 flakes can display a formate generation rate of 1.9 μmol g^{-1} h^{-1} under ultraviolet light irradiation, roughly 450 times relative to bulk TiO_2. Unfortunately, this works lack of the study of oxidation half reaction, authentic carbon source exploration, and longer time cycle tests. Although increased CO_2 photoreduction activity can be acquired over ultrathin TiO_2 flakes, the formate generation rate is quite low and the TiO_2 can only response to ultraviolet light, which greatly limit the possible applications.

To extend the optical response range and boost the CO_2 photoreduction activity, bismuth-based materials such as BiOBr, $Bi_4O_5Br_2$ are developed. For example, Xie et al. demonstrated the single unit cell Bi_2WO_6 layers can achieve excellent photoreduction performance to convert CO_2 to methanol [53]. Through a lamellar hybrid intermediate strategy, the Bi_2WO_6 layers with thickness as low as 1.65 nm can be prepared. On the basis of density-functional-theory (DFT) calculations, the dominating charge density located at the surface of Bi_2WO_6 layers, suggesting the ultrathin thickness bring about more active electrons. Thus, the Bi_2WO_6 layers displays much increased conductivity than that of bulk Bi_2WO_6, as proved by temperature-dependent resistivities and time-resolved fluorescence spectroscopy. Coupled with the features of larger CO_2 adsorption capacity and higher photoabsorption, the Bi_2WO_6 layers can deliver a methanol formation rate of 75 μmol g^{-1} h^{-1} under 300 W Xe lamp irradiation, which is 125 times relative to bulk Bi_2WO_6. The consecutive cycling tests up to 36 h do not show obvious activity decay, suggest the excellent photostability. However, no $^{13}CO_2$ labeling experiment is performed to trace the carbon source of methanol.

To further extend the light harvesting scope to near-infrared or infrared region, several systems are explored [40,42]. For example, metallic CuS atomic layers with two-unit-cell thickness are prepared with the assistance of oleylamine and octylamine (Fig. 2) [42]. The low electrical resistance in the whole temperature range and valence band (VB) maximum passes through the Fermi level (0 eV), together revealing the metallic character of CuS atomic layers, also certified by DFT calculations. The CuS atomic layers display strong light absorption from ultraviolet to infrared region, with the absorption energy gap about 1.01 eV. Benefiting from the intraband transition among CB and the interband transition from CB to B_1 band, CuS atomic layers can achieve CO_2 reduction and H_2O oxidation simultaneously under IR light irradiation. As a result, a CO production rate of 14.5 μmol g^{-1} h^{-1} with near 100% selectivity can be realized over CuS atomic layers under IR light, whereas CuS bulk display almost no IR light catalytic activity. The AQY of CuS atomic layers can reach 0.05% at 800 nm. $^{13}CO_2$ and $H_2^{18}O$ labeling experiments suggest the CO and O_2 are stemmed from CO_2 photoreduction with the assistance of H_2O, with the stoichiometric ratio of produced CO and O_2. Moreover, no obvious activity loss of CuS atomic layers can be seen under IR light irradiation for 96 h. In situ FT-

IR spectra study indicate the gradually appeared and strengthened signal at 1545 cm^{-1} with extended irradiation time, which is ascribed to the typical intermediate of COOH* for CO formation. This work demonstrates the possible of ultrathin conductor materials for IR light driven photocatalysis, such as metal sulfides, selenides, nitrides and phosphides.

3.3. 3D assembled ultrathin structure

Apart from freestanding 1D, 2D ultrathin structures, the 3D structure with the assembly of ultrathin structures can also exhibit outstanding photocatalytic performance towards CO_2 reduction [57–61].

Zou et al. demonstrated the UV-light-responsive ultrathin $ZnGa_2O_4$ nanosheet scaffolds can effective convert CO_2 into CH_4 [61]. Yu et al. prepared 3D $g-C_3N_4$ hierarchical structure with ultrathin nanosheets (~3 nm) assembly through stepwise NH_3-mediated thermal exfoliation process [60]. Compared with bulk $g-C_3N_4$, it displays greatly improved light absorption, higher redox potential, more effective charge separation and larger CO_2 adsorption capacity. As a result, the 3D $g-C_3N_4$ hierarchical structure can reduce CO_2 into CH_4 (1.39 μmol g^{-1} h^{-1}) and CH_3OH (1.87 μmol g^{-1} h^{-1}) under light irradiation, which are 10 and 5 times higher than that of bulk $g-C_3N_4$, respectively.

To further boost the CO_2 photoreduction efficiency, Lou et al. prepared hierarchical $In_2S_3-CdIn_2S_4$ heterostructured nanotubes consist of ultrathin nanosheets (Fig. 3) [57]. With the help of $Co(bpy)_3^{2+}$ as cocatalyst, acetonitrile to promote CO_2 dissolution, and TEOA as electron donor, the as-prepared $In_2S_3-CdIn_2S_4$ can display outstanding performance to reduce CO_2 into CO under visible light irradiation. The optimal CO production rate can arrive 825 μmol g^{-1} h^{-1}, significantly higher than that of In_2S_3 and $CdIn_2S_4$. The effective separation of charge carriers, increased CO_2 adsorption and more active sites in $In_2S_3-CdIn_2S_4$ joint guarantee the excellent performance. It's worth noting that the product selectivity should be further improved since plentiful H_2 is produced in this system. Following the above strategy, the same group further develop $ZnIn_2S_4-In_2O_3$ hierarchical tubular with $ZnIn_2S_4$ nanosheets on the surfaces of In_2O_3 and nitrogen-doped carbon@$NiCo_2O_4$ (NC@$NiCo_2O_4$) double-shelled nanoboxes for CO_2 photoreduction [58,59]. The CO-evolving rate can be improved to amazing 3075 and 26,200 μmol g^{-1} h^{-1}, respectively. The NC@$NiCo_2O_4$ with the highest activity possess the AQY of 1.07% under 420 nm. Despite the excellent performances, several issues still need to be made clear in these systems. The actual role of $Co(bpy)_3^{2+}$, acetonitrile, TEOA should be further carefully explored. Whether these carbonic species provide the carbon source for products. What are the final structures of these carbonic species after long time reaction? Meanwhile, the amount of catalyst is only 1 or 4 mg, which is too low to guarantee the authenticity after the rate conversion to per gram.

4. Tailoring strategies of performance

To further optimize the CO_2 photoreduction performance of ultrathin structures, several strategies have been employed through tuning the surface coordination structure, electronic structure, carrier concentration, charge separation and so on.

4.1. Atomic incorporation

Atomic incorporation is an efficient strategy to tune the local surface microstructure and electronic structure of materials with maintaining the ultrathin structures. The atomic types, distribution locations, and diverse concentrations of the incorporated atoms will have great effect on the properties of the ultrathin structured photocatalysts.

First of all, nonmetal incorporation is an effective method to boost the photocatalytic behavior through extending the light harvesting scope and tuning the carriers transport. According to the form of surface incorporation or bulk incorporation, varied electronic structure
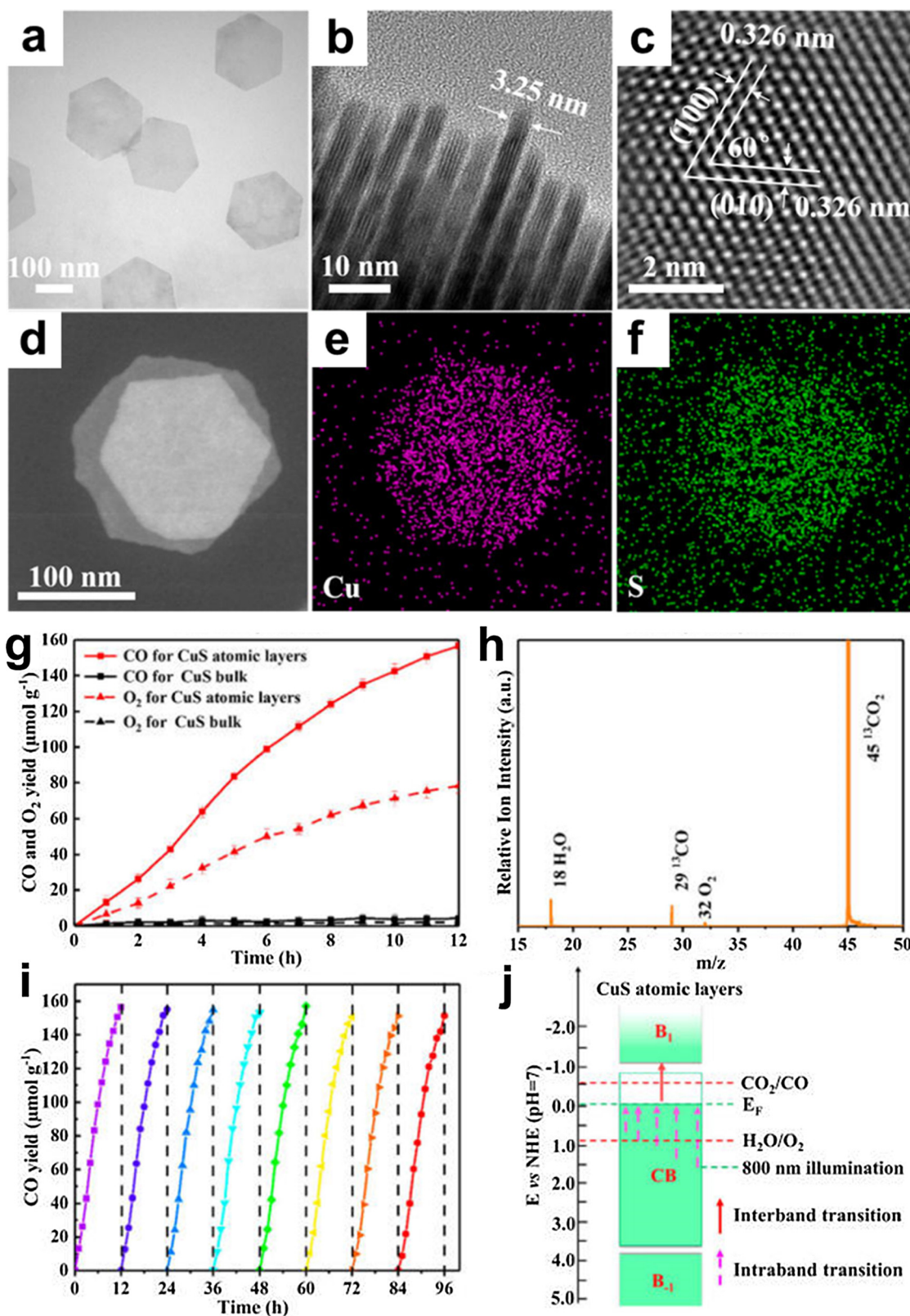
Fig. 2. (a) top view and (b) side view of TEM images, (c) HRTEM image, (d–f) annular dark-field TEM images and the corresponding elemental mapping images of CuS atomic layers, (g) products of photocatalytic CO_2 reduction, (h) SVUV-PIMS spectrum of the products after $^{13}CO_2$ photoreduction for the CuS atomic layers, (i) cycling measurements, (j) electronic band structures of the CuS atomic layers, reproduced with permission from ref. [42], American Chemical Society.

can be observed with impurity energy level in the band gap or entirely elevate the VB edge. As a consequence, the corresponding varied light harvesting performance is create shoulder, trail peaks in absorption spectrum and entirely red shifting the light absorption edge. For

instance, Wang et al. incorporate C into h-BN to build BCN alloy ultrathin nanosheets (Fig. 4) [62]. According to the DFT calculations, h-BN possesses an indirect bandgap of 4.56 eV with N 2p orbit mainly contribute to the donor level and B 2p orbit dominate the acceptor
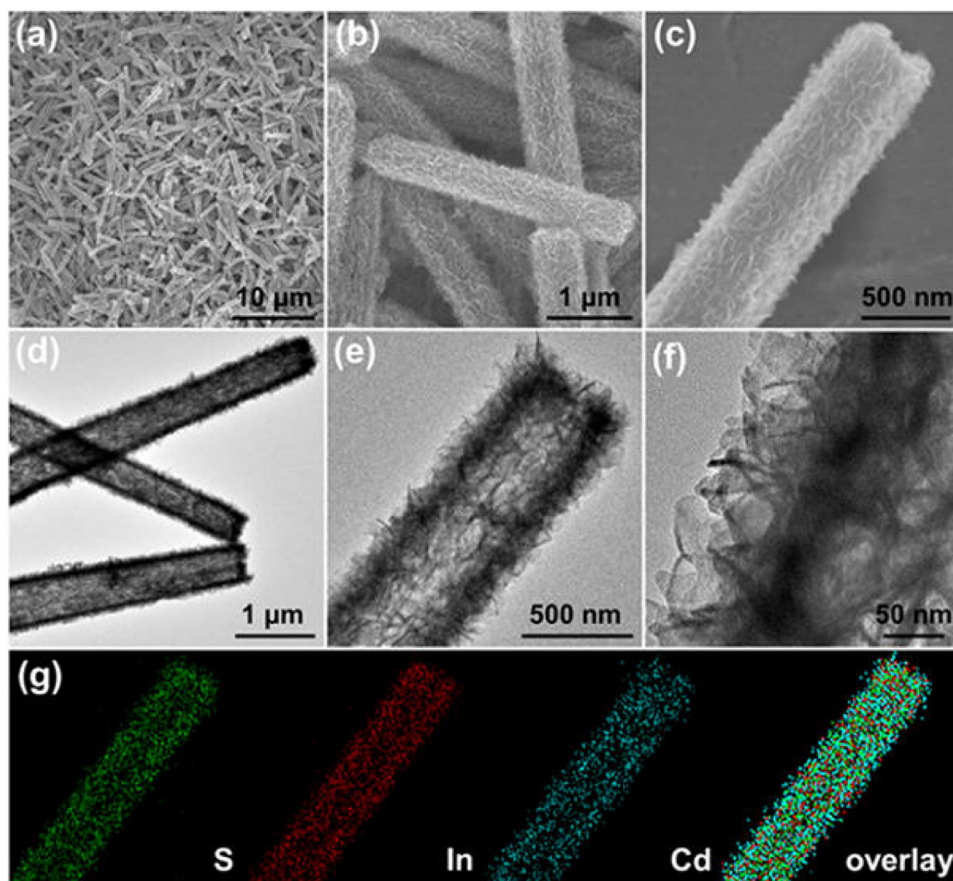
Fig. 3. (a–c) SEM and (d–f) TEM images of In_2S_3-$CdIn_2S_4$-10 nanotubes, and (g) elemental mappings of a single In_2S_3-$CdIn_2S_4$-10 nanotube, reproduced with permission from ref. [57], American Chemical Society.
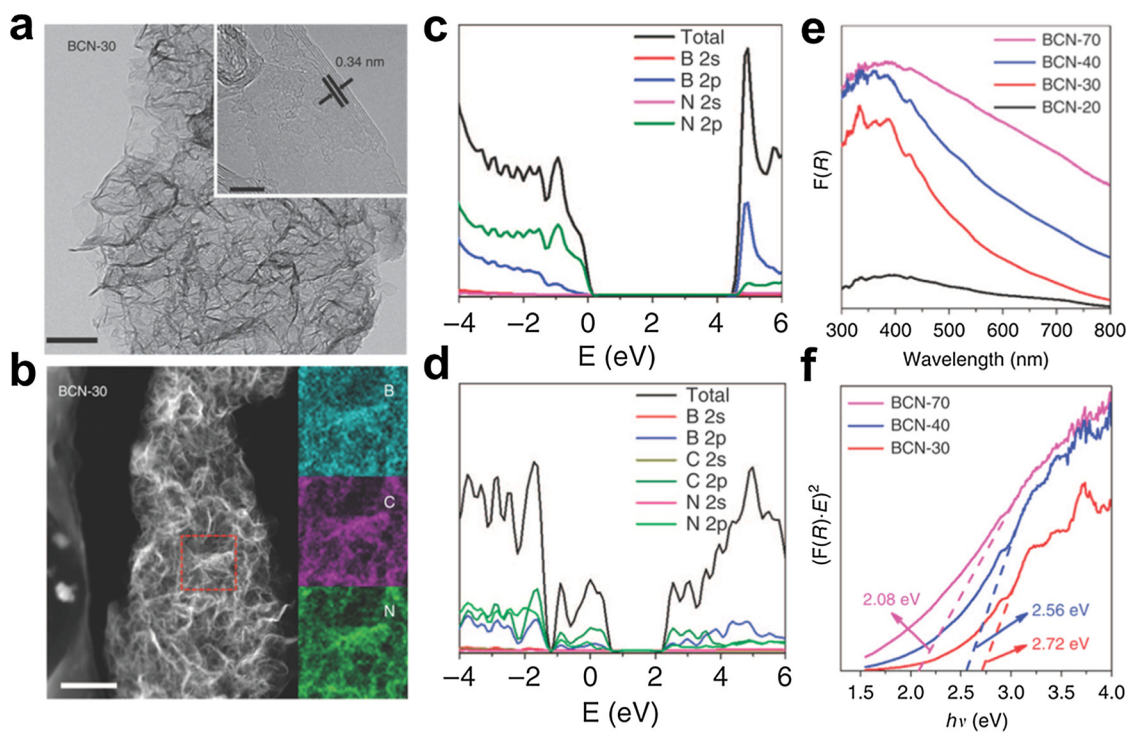

Fig. 4. (a) HRTEM image of the BCN-30 sample. Scale bar, 100 nm, inset scale bars, 5 nm. (b) Typical TEM dark-field image of BCN-30 sample and the elemental mapping images. Scale bar, 300 nm. Electronic density of states of (c) $B_{16}N_{16}$ and (d) $B_{11}C_{12}N_9$. (e) UV–vis DRS and (f) bandgap of the BCN-x samples. Reproduced with permission from ref. [62], Nature Publishing Group.

level. After incorporation of C, the band gap of $B_{11}C_{12}N_9$ can be reduced to 2.00 eV with C 2p orbitals dominate the VB and CB edges. This tuned electronic structure can be finely reflected in ultraviolet-visible diffuse reflectance spectra with band gap decreased to 2.08 eV. Benefiting from the greatly reduced band gap, the optimized BCN-30 nanosheets can response to visible light and thus can deliver a CO_2 photoreduction behavior to produce CO under visible light irradiation. Apart from single element incorporation, multielement co-incorporation can also effective tailor the CO_2 photoreduction behavior. By simultaneous incorporating C and N into sodium titanate nanotubes (C,N-TNT), the energy band structure can be effective adjusted [31]. The C,N-TNT with an intermediate incorporation concentration can result in the maximum methane yield rate of 9.75 $\mu mol\,g^{-1}\,h^{-1}$.

In addition to nonmetal incorporation, metal atoms incorporation can display unique features due to the diversified electron configurations and orbits. Wang et al. demonstrated the incorporation of Mo into Mo-WO_3·0.33H_2O nanorods can dramatically improve the CH_4 production rate from 1.02 to 5.3 $\mu mol\,g^{-1}\,h^{-1}$ [33]. Profiting from the ability to store and localize photoinduced electrons, the Mo atoms can facilitate CO_2 activation and promote the electron transfer to adsorbed CO_2 molecules, contributing to the increased photoreduction performance. The same group also incorporate Co into $BiVO_4$ atomic layers to promote the CO_2 reduction efficiency [63]. The Co atoms can increase the electron densities around O in $BiVO_4$, which further facilitate CO_2 activation and electron transfer to CO_2. As a result, optimized CH_4 production rate of 23.8 $\mu mol\,g^{-1}\,h^{-1}$ can be achieved under atmospheric CO_2 concentration (400 ppm). Apart from activity tuning, the atomic incorporation can also adjust the selectivity in CO_2 photoreduction. For instance, Liu et al. prepared Ni doped $ZnCo_2O_4$ atomic layers through CTAB assisted solvothermal process [64]. On the basis of DFT calculation, the Ni atoms build several new energy levels in the band gap and increases the DOS at the CB minimum. Study found that the doped Ni atoms is beneficial to the desorption of CO, while pure $ZnCo_2O_4$ favors the CH_4 desorption. Thus, the Ni-doped $ZnCo_2O_4$ atomic layers display 3.5 times higher CO selectivity than pure $ZnCo_2O_4$, with CO and CH_4 generation rates of 31.4 and 20.2 $\mu mol\,g^{-1}\,h^{-1}$. The $CO_2^{\cdot-}$ radical is determined to be the main intermediate during the CO_2 reduction process. What's more, the simultaneous metal and nonmetal incorporation or atomic pair incorporation may also paly tremendous role in taming CO_2 photoreduction performance. All the results undoubtedly indicate that the atomic incorporation is an appealing strategy to tune the carries concentration, energy band structure of ultrathin photocatalysts and can further promote the CO_2 photoreduction performance.

4.2. Vacancy engineering

Vacancy engineering has been testified as a versatile method to maneuver the photocatalytic performance towards CO_2 conversion [65,66]. When the thickness decreased to atomic ultrathin, the finite material size will lead to crystal discontinuity and thus atom vacancies with surrounding dangling bonds will easy appear at surfaces, which demonstrate the probability to modulate the electronic structure, electron transport and surface catalysis process [67]. Up to now, many anion or cation vacancies-tuned ultrathin structures have been reported towards CO_2 photoreduction, such as V_O-ZnAl LDH, V_O-$Bi_{12}O_{17}Cl_2$, V_O-BiOBr, V_O-WO_3, V_O-Bi_2WO_6, V_{Bi-O}-Bi_2MoO_6, V_{Zn}-$ZnIn_2S_4$, V_V-$BiVO_4$, and so on [30,40,45,47,54,66,68,69].

Firstly, the charge separation efficiency in ultrathin materials can be effective tuned by formed surface vacancies. Xie et al. engineered Zn vacancies into one-unit-cell $ZnIn_2S_4$ layers, as soundly certified by directly observation through aberration-corrected high-angle annular dark-field scanning transmission electron microscopy (HAADF-STEM, Fig. 5a–f) [45]. The Zn vacancies can serve as trap centers for photogenerated electrons. As a consequence, the electron-hole pair separation efficiency in V_{Zn}-$ZnIn_2S_4$ can be greatly improved and boost the

CO_2 reduction to yield CO, reach 33.2 $\mu mol\,g^{-1}\,h^{-1}$. The AQY of V_{Zn}-rich $ZnIn_2S_4$ is determined to be 0.23% at 400 nm. Control experiments in N_2 or in dark or without photocatalysts did not show CO formation, demonstrating that the CO formation was come from photoreduction of CO_2. $^{13}CO_2$ labeling experiment indicate the dominant product was ^{13}CO ($m/z = 29$), firmly prove the CO was derived from CO_2 photoreduction. After 24 h CO_2 photoreduction reaction, the TEM images, XRD patterns, EPR and XPS spectra of the used sample did not show obvious variations, further strongly confirmed the stabilized catalytic reaction. Through the artificial lamellar hybrid precursors, the $BiVO_4$ atomic layers with rich or poor vanadium vacancies can be controlled prepared (Fig. 5g–k) [54]. The vanadium vacancies is well testified by positron annihilation spectrometry (PAS). The engineered vacancies can tune the electronic structure of $BiVO_4$ by create defect level in band gap and increase the DOS near Fermi level. The vanadium vacancies in V_V-$BiVO_4$ is demonstrated to be able to increase photoabsorption, electronic conductivity and carrier lifetime, so as to promote the CO_2 photoreduction performance. The methanol formation rate can arrive 398.3 $\mu mol\,g^{-1}\,h^{-1}$, with the AQY of 5.96% at 350 nm, which is among the highest rates for methanol formation in ultrathin materials. The hole can oxidize H_2O into O_2, with the produced rates of O_2 : CH_3OH is 1.5, meet the theoretical stoichiometric ratio. The activity of V_V-$BiVO_4$ did not show any deterioration during 4 day cycles. The structures of V_V-$BiVO_4$ did not show distinct variation, as proved by XRD patterns and Raman spectra. All these results indicate the stable CO_2 photocatalytic reduction yield CH_3OH process over V_V-$BiVO_4$.

Apart from charge separation efficiency and electronic conductivity tuning, the surface vacancies can also serve as activation center for CO_2 moleculars. For instance, Zhang et al. engineered O vacancies into ZnAl LDH ultrathin nanosheets to form Zn^+-V_O complexes (Fig. 6a–c) [47]. The formed vacancy structure is well proved by electron paramagnetic resonance (EPR), X-ray absorption fine structure (XAFS) coupled with PAS. The created Zn^+-V_O complexes can work as trapping sites to promote the adsorption and activation of CO_2 and H_2O molecules. As a result, the V_O-ZnAl LDH can effective reduce CO_2 to CO (7.6 $\mu mol\,g^{-1}\,h^{-1}$) under UV–vis light. $^{13}CO_2$ labeling experiment confirm that CO is originate from CO_2 photocatalytic reduction over V_O-ZnAl-LDH. The CO_2 photoreduction stability of sample can maintained up to at least 30 h.

Moreover, in some systems, the engineered surface vacancies can simultaneous optimize the photoabsorption, charge separation and CO_2 activation process. For instance, O vacancies in single unit cell BiOBr is demonstrated to be able to boost the CO_2 reduction behavior from these three aspects (Fig. 6d–f) [68]. First of all, the O vacancies in BiOBr atomic layers can create some new defect levels in band gap, which enable the acquirement of narrowed band gap, as certified by UV–vis diffuse reflectance spectra. Secondly, the engineered O vacancies can effective promote the charge separation, as proved by the increased carrier lifetime from 0.5 to 3.12 ns. Thirdly, the charge delocalization around the O vacancies favors the activation of CO_2 and facilitates CO_2 conversion into COOH* intermediate. Benefiting from these features, the V_O-BiOBr atomic layers delivers a CO production rate of 87.4 $\mu mol\,g^{-1}\,h^{-1}$ under visible light irradiation, roughly 20 times higher than perfect BiOBr atomic layers. A strong signal at $m/z = 29$ which ascribed to ^{13}CO can be observed in mass spectrometry by using $^{13}CO_2$ as source, suggesting the CO is come from CO_2 photoreduction. The nearly 2:1 ratio of the produced CO : O_2 reveal the ideal $2CO_2 \rightarrow 2CO + O_2$ process. 60 h long time tests did not display any activity loss, and phase, morphology, and oxygen vacancies similarly maintain unchanged, associated suggest the good photocatalytic stability.

Based on the above results, it can be found that electronic structure, light absorption, electron transfer process can be tune by vacancy engineering. The local charge density at the surface can also be adjusted and may favors the adsorption and activation of CO_2 molecules and facilitate interfacial reactions. However, there are still some issues worth noting for the CO_2 photoreduction process over vacancy-rich
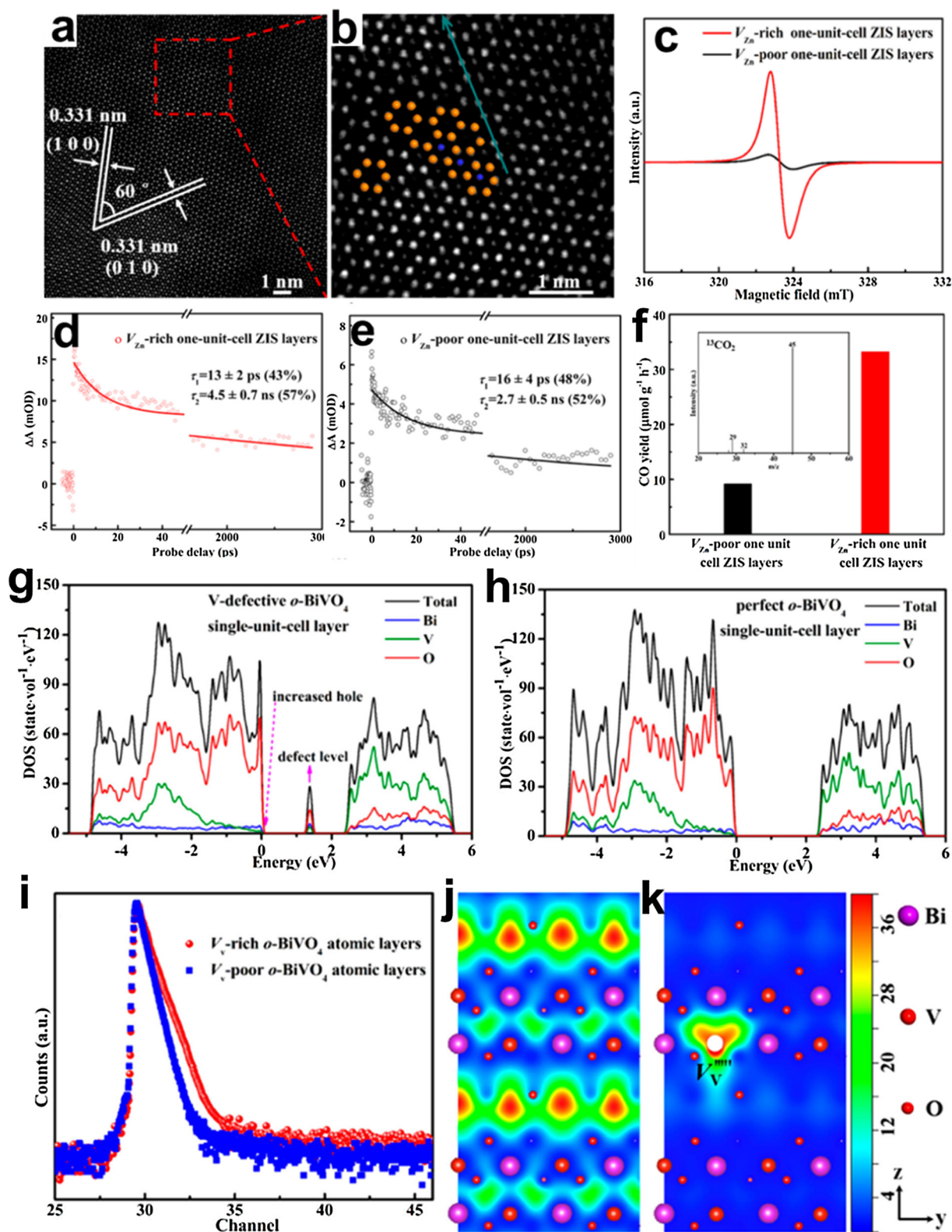
Fig. 5. (a, b) HAADF-STEM images of V_{Zn}-ZnIn$_2$S$_4$, (c) EPR spectra of ZnIn$_2$S$_4$ layers. Ultrafast TA spectroscopy of (d) V_{Zn}-ZnIn$_2$S$_4$ and (e) V_{Zn}-poor ZnIn$_2$S$_4$ layers. (f) Photoreduction of CO$_2$ into CO over ZnIn$_2$S$_4$ layers. Calculated density of states of (g) V_V-rich BiVO$_4$ and (h) perfect BiVO$_4$ layer. (i) Positron lifetime spectrum, (j, k) schematic representation of trapped positrons over V_V-rich and Vv-poor BiVO$_4$ layers. reproduced with permission from refs. [45,54], American Chemical Society.

ultrathin materials. In some systems, the vacancy in materials could accelerate the charge recombination, which is the disadvantage for photocatalytic process. During CO$_2$ photoreduction process, the similar effect may also exist, thus it is necessary to clarify the veritable role of

vacancies for charge separation in different systems. In addition, the surface vacancies, such as oxygen vacancies, may directly involve in the interfacial reactions for CO$_2$ activation and conversion in some systems. It is desirable to explore the variation or loss of oxygen vacancies during
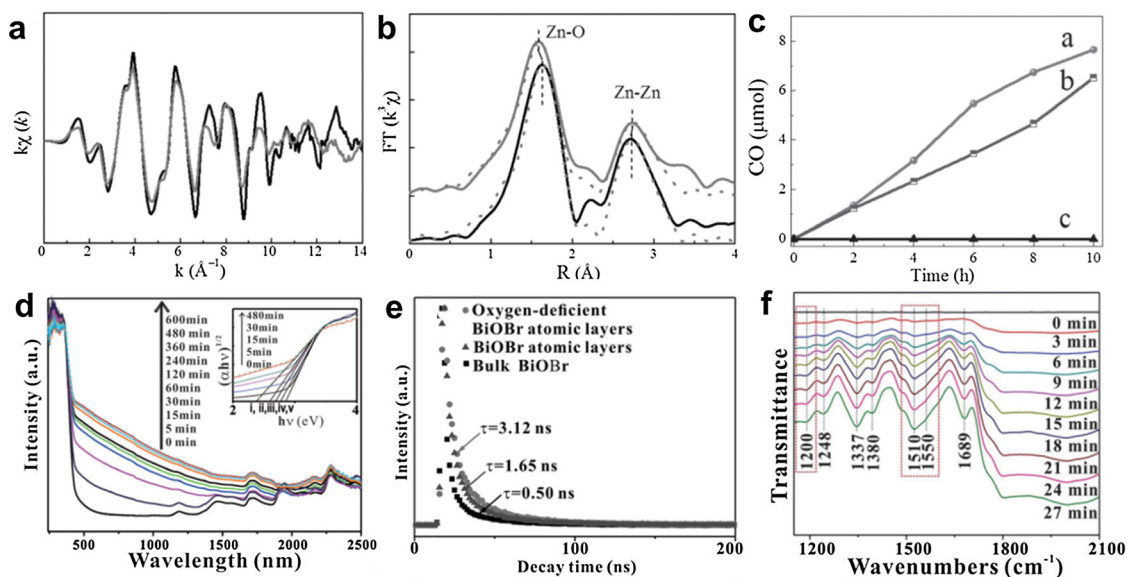
Fig. 6. (a) Zn K-edge extended XANES and (b) magnitude of k^2-weighted FT of Zn K-edge EXAFS spectra for ZnAl-1 (gray), ZnAl-3 (black). (c) Photoreduction over different ZnAl LDH. (d) UV/vis DRS for BiOBr atomic layers after various time of UV irradiation. (e) Fluorescence emission decay spectra of BiOBr materials. (f) In situ FTIR spectra for coadsorption of a mixture of CO_2 and H_2O vapor over V_O-BiOBr atomic layers. reproduced with permission from ref. 47, Wiley-VCH and ref. [68], American Chemical Society.

the reduction process, so as to make it clear of the interface catalysis mechanism.

4.3. Crystal facet tailoring

Different crystal facets possess diverse surface atomic structures such as atomic coordination and arrangement, which can determine the adsorption states and interaction with CO_2 molecules [70]. Moreover, the various crystal facets with specific surface configuration will bring about multifarious surface energies, which significantly affect the migration and accumulation of electrons and holes to trigger specific redox reactions [71]. Tang et al. prepared Co_3O_4 hexagonal platelets with (112) or (111) exposed facets through the conversion from Co$(OH)_2$ at 400 or 800 °C, respectively (Fig. 7) [72]. DFT calculations are performed to study the adsorption and dissociation of CO_2 for the reduction to yield CO on (112) or (111) exposed facets of Co_3O_4. On (111) facet of Co_3O_4, the configuration of CO_2* is one O atom coordinated with one Co atom, with the O-Co bond length of 2.28 Å. However, on (112) facet, CO_2* situates at the middle of 3-coordinated and 2-coordinated Co atoms, forming C-Co bond length of 1.87 Å and O-Co bond length of 2.00 and 2.01 Å, respectively. Thus, the (112) exposed facet displays much larger adsorption energy of CO_2* than (111) exposed facet (-1.69 vs. -0.13 eV). Further study found the free energy change from CO_2* to COOH* is 0.48 and 0.32 eV on (111) and (112) facet, respectively, which reveal the increased stability of COOH* on (112) facet. Benefiting from the optimized surface configuration, the (112) facet exposed Co_3O_4 platelets can deliver a CO formation rate of 2003 μmol g^{-1} h^{-1} with the assistance of [Ru(bpy)$_3$]Cl$_2$ photosensitizers, much higher than that of (111) facet exposed Co_3O_4 platelets (1238 μmol g^{-1} h^{-1}). The AQY can arrive 0.069% at 450 nm. Similarly, Ye et al. demonstrated the facet-dependent CO_2 photoreduction activity over BiOI nanosheets [52]. Profiting from the unique atomic configuration, the upshifted CB potential of (001) facet can be achieved and thus the more reductive electrons can be produced. Meanwhile, the
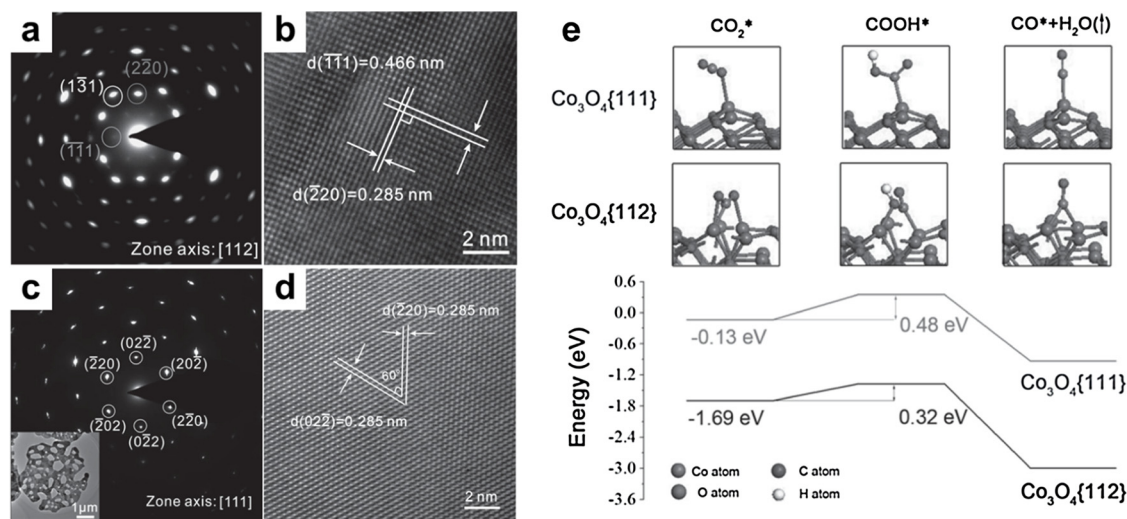

Fig. 7. (a) SAED and (b) HRTEM images of Co_3O_4 platelets with (112) facet exposure. (c) SAED, TEM (insert) and (d) HRTEM images of Co_3O_4 platelets with (111) facet exposure. (e) DFT calculation of adsorption and reduction of CO_2 on Co_3O_4 surfaces. Free energy diagram of the COOH* intermediate during CO_2 reduction process on (111) and (112) surfaces of Co_3O_4 platelets. reproduced with permission from ref. [72], Wiley-VCH.

self-induced internal electric field is perpendicular BiOI-001 but parallel to BiOI-100 according to the (001) and (100) atomic structure, which is more beneficial to the charge separation in BiOI-001. Therefore, the BiOI-001 nanosheets can display increased CO_2 photoreduction performance for the production of both CO and CH_4.

Apart from the tailoring of various crystal facets, the synergetic utilization of diverse crystal facets may also an effective strategy to further boost the CO_2 photoreduction. Study found the ratio of (001) and (101) facets of TiO_2 play important role to the CO_2 reduction activity [73]. Since the (001) and (101) facets of TiO_2 have diverse atomic configuration and band edge positions, the electrons and holes prefer to transfer to the (101) and (001) facets, respectively. Thus, a surface junction can be built with optimal ratio of the exposed (101) and (001) facets in 45:55 to display the maximized CH_4 formation rate. Refer to this strategy, the CO_2 photoreduction performance may also be greatly promoted through ratio adjust of exposed facets in ultrathin materials. The optimized charge separation can be acquired among different crystal facets due to differentiated energy band structures, finally boost the CO_2 photoreduction behavior.

4.4. Surface modification

To further boost the activity, product selectivity and stability of the ultrathin structures, surface modification with suitable cocatalysts is an appealing strategy. Several roles of cocatalysts have been acquired in different photocatalytic CO_2 reduction systems, such as promote surface charge separation, lower the activation energy, improve selectivity to yield specific molecules and increase the stability by timely consume overmuch carriers [74].

Up to now, several types of cocatalysts have been successfully developed to boost the CO_2 photoreduction performance of ultrathin structures, such as noble metal (Pt-based, Pd-based, Ru-based, Rh-based), noble metal-free (Cu-based, Bi-based), alloys, metal-free (graphene-based, carbon quantum dots-based) [75–90]. Pt-based cocatalysts are employed by Liu et al. and Wang et al. to boost the CO_2 reduction behavior over ultrathin TiO_2 and ultrathin Bi_2WO_6 nanosheets, respectively [75,76]. The ultrafine Pt nanoparticles induces the efficient separation of charge carriers in TiO_2 and promote the adsorption of CO_2, contribute to the higher generation rate of CH_4 and CO. While the PtO_x nanoparticles on Bi_2WO_6 can accelerate the water oxidation process, so as to promote the yield rate of CH_4 to 108.8 ppm $g^{-1}h^{-1}$ (10.7 $\mu mol\,g^{-1}\,h^{-1}$). The Pd-based cocatalysts are widely used to increase the CO_2 reduction over ultrathin structures. Bai's et al. prepared Pd nanosheets modified TiO_2 nanosheets with various size of Pd nanosheets [78]. It can be found that small Pd nanosheets with higher edge density can realize higher photocatalytic activity over TiO_2 nanosheets, revealing the edges of Pd nanosheets serving as the highly active sites towards CO_2 reduction reaction. To further increase the edge sites of cocatalysts, Rh and Pd nanowires with abundant grain boundary are modified on TiO_2 nanosheets [81]. Through accelerating the interfacial electron transfer from TiO_2 to metal cocatalysts and grain boundaries act as active sites, the CO_2 photoreduction activity can be improved and H_2 evolution side reaction can be suppressed. At the same time, varied exposed facets of cocatalysts can also have effect on the performance optimizing. Through the crystalline phase controlling, Ru nanocrystals in face-centered cubic (fcc) phase with dominated (111) facet and hexagonal close-packed (hcp) phase with dominated (1011) facet are modified on C_3N_4 nanosheets [80]. Study found that the adsorption energy of CO_2 molecules on (1011) facet is higher than that of (111) facet, so as stronger interaction can be built between CO_2 molecules and hcp Ru. As a consequence, the activity and selectivity of C_3N_4-hcp Ru can be increased towards CO_2 reduction.

With respect to noble metal-free cocatalysts, Cu-based materials have been regarded as effective alternative for CO_2 reduction. Miyauchi et al. modified amorphous copper oxide (Cu(II)) nanoclusters on $Nb_3O_8{}^-$ nanosheets to boost the CO_2 conversion to yield CO [82].

Through ESR analysis coupled with $H_2{}^{18}O$ and $^{13}CO_2$ isotope labeling experiments, it is demonstrated that H_2O molecules afford electrons and be excited by photon energy. The Cu(II) nanoclusters can serve as reservoir to trap photogenerated electrons and work as active sites to yield CO molecules. Apart from nanoclusters, recent studies found single atoms are excellent cocatalysts to tune the photocatalytic behavior [91,92]. The single atom catalysts (SAC) can enable reasonable use of metal resources and facilitate atomic economy through maximum atom-utilization efficiency. The unique electronic structure and low-coordinated environment make the single atoms to be highly active sites with favorable selectivity. For instance, Wu et al. modified isolated Bi on TiO_2 nanosheets via a simple ionic adsorption method for CO_2 photoreduction [84]. The engineered Bi single atoms can create a built-in electric field in TiO_2, promoting the separation of charge carriers. The Bi single atoms can not only increase the CO_2 reduction activity but also improve the selectivity to yield CH_4. Our group developed Co single atoms tuned Bi_3O_4Br atomic layers for CO_2 photoreduction [91]. The engineered Co single atoms favors the charge transition, carrier separation, and CO_2 activation, as proved by ultrafast transient absorption (TA) spectra, in situ FTIR and theoretical calculation. Benefiting from the advantages of Co single atoms and 2D ultrathin structure, the Co-Bi_3O_4Br can deliver a CO formation rate of 107.1 $\mu mol\,g^{-1}$ h^{-1}. $^{13}CO_2$ isotopic labeling experiment is conducted to prove the carbon source of CO is CO_2.

Through the alloying of noble metal or non-noble metal, the effect of cocatalysts can be further tuned and better boost CO_2 photoreduction behavior [86–88]. Xiong's et al. developed CuPd alloy cocatalysts by isolating Cu atoms in Pd lattice and modified on TiO_2 nanosheets for highly selective reduce CO_2 into CH_4 (Fig. 8) [85]. The isolated Cu atoms is determined by STEM and EXAFS spectra and Pd_7Cu_1 displays the optimal co-catalysis role, which can deliver a 96% high selectivity for CH_4 production with a rate of 19.6 $\mu mol\,g^{-1}\,h^{-1}$. The isolated Cu atoms in Pd lattice plays crucial roles for CO_2 reduction optimizing. It not only affords the paired Cu-Pd sites to increase CO_2 adsorption and restrain H_2 evolution, but also elevates the d-band center of Cu sites for better CO_2 activation.

Apart from metal cocatalysts, metal-free materials such as graphene, carbon quantum dots (CQDs) are alternative to work as cocatalysts to boost the CO_2 photoreduction reactions [93,94]. For instance, Kong et al. employ CQDs to modify the ultrathin Bi_2WO_6 nanosheets (UBN) and found the CQDs can effective improve the CH_4 production rate under visible light irradiation [89]. Meanwhile, the CQDs/UBN can realize NIR-driven CO_2 reduction due to the excellent spectral coupling of UBW and CQDs, and the generated up-converted photoluminescence by CQDs. All these results demonstrated that by tuning the surface modified cocatalysts with the maintain of ultrathin structure of subject photocatalysts is an effective tool to tune the electronic structure and surface property of ultrathin photocatalysts and can further promote the photocatalytic CO_2 reduction.

4.5. Heterostructure construction

Building semiconductor heterostructure is a promising strategy to enhance the photocatalytic activity, owing to the tunable band structures of multiple components and efficient electron-hole separation, which afford them with suitable properties exceed to the individual components [95]. With respect to ultrathin structures for CO_2 photoreduction, several types of heterostructures have been developed successfully with improved photocatalytic performance, such as particle coupling heterojunction [96–100], 2D/2D heterojunction [101–103], in-plane heterojunction [43] and Z-scheme system [104–107].

4.5.1. Particle coupling heterojunction

Coupling nanoparticle with ultrathin materials is an appealing method to promote the CO_2 photoreduction rate. Wang et al. coupled CdS nanoparticles with BCN nanosheets to construct matched energy
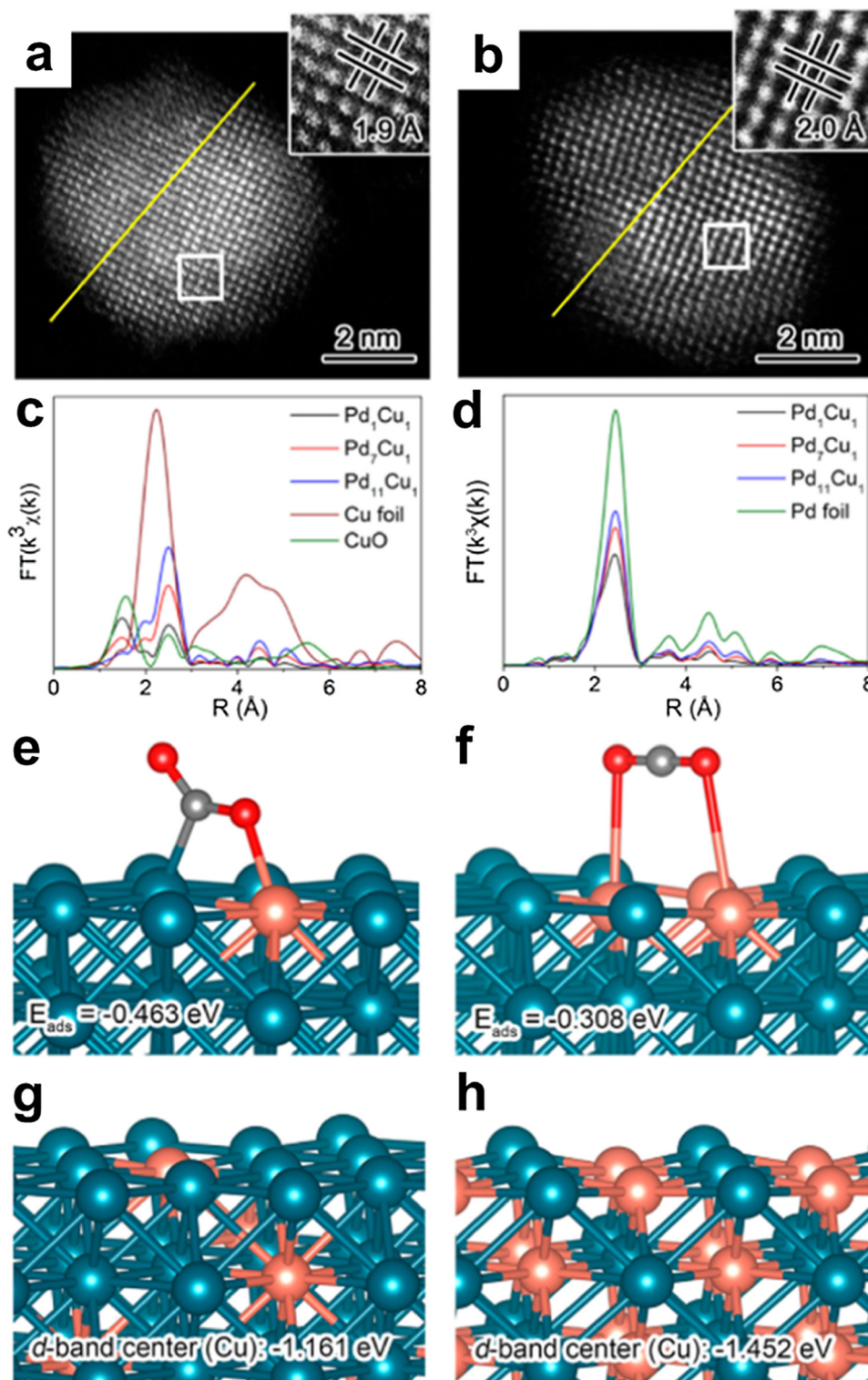
Fig. 8. HAADF-STEM images of (a) Pd_1Cu_1 and (b) Pd_7Cu_1. k^3-weighted Fourier-transform (c) Cu K-edge and (d) Pd K-edge EXAFS spectra. Most favorable configurations and adsorption energies of CO_2 at (e) an isolated Cu atom, and (f) two neighbored Cu atoms. The structural models and Cu d-band centers for ordered (g) Pd_7Cu_1 and (h) Pd_1Cu_1 lattices. reproduced with permission from ref. [85], American Chemical Society.

band structure [98]. The photogenerated electrons on the CB of CdS will tend to transfer to the CB of BCN, while the holes will migrate from the VB of BCN to that of CdS, building effective charge separation. With the help of TEOA as the reducing agent to consume holes, the CdS/BCN displays a considerable CO generation rate of $250 \, \mu mol \, g^{-1} \, h^{-1}$, 10-fold higher than pure BCN. Similarly, Ye et al. coupled UiO-66 with C_3N_4 nanosheets to build heterostructures [96]. Study found the

electrons from the excited C_3N_4 nanosheet will transfer to UiO-66, enabling the substantially restraint of carriers recombination in C_3N_4. As a result, the long-lived electrons in UiO-66/C_3N_4 can supply 3.4 time increased CO formation rate relative to C_3N_4. Although the increased performance can be obtained, the limited dispersion of nanoparticle lower the contact area between two types of materials, which hamper the charge transfer process and cannot achieve sufficient charge
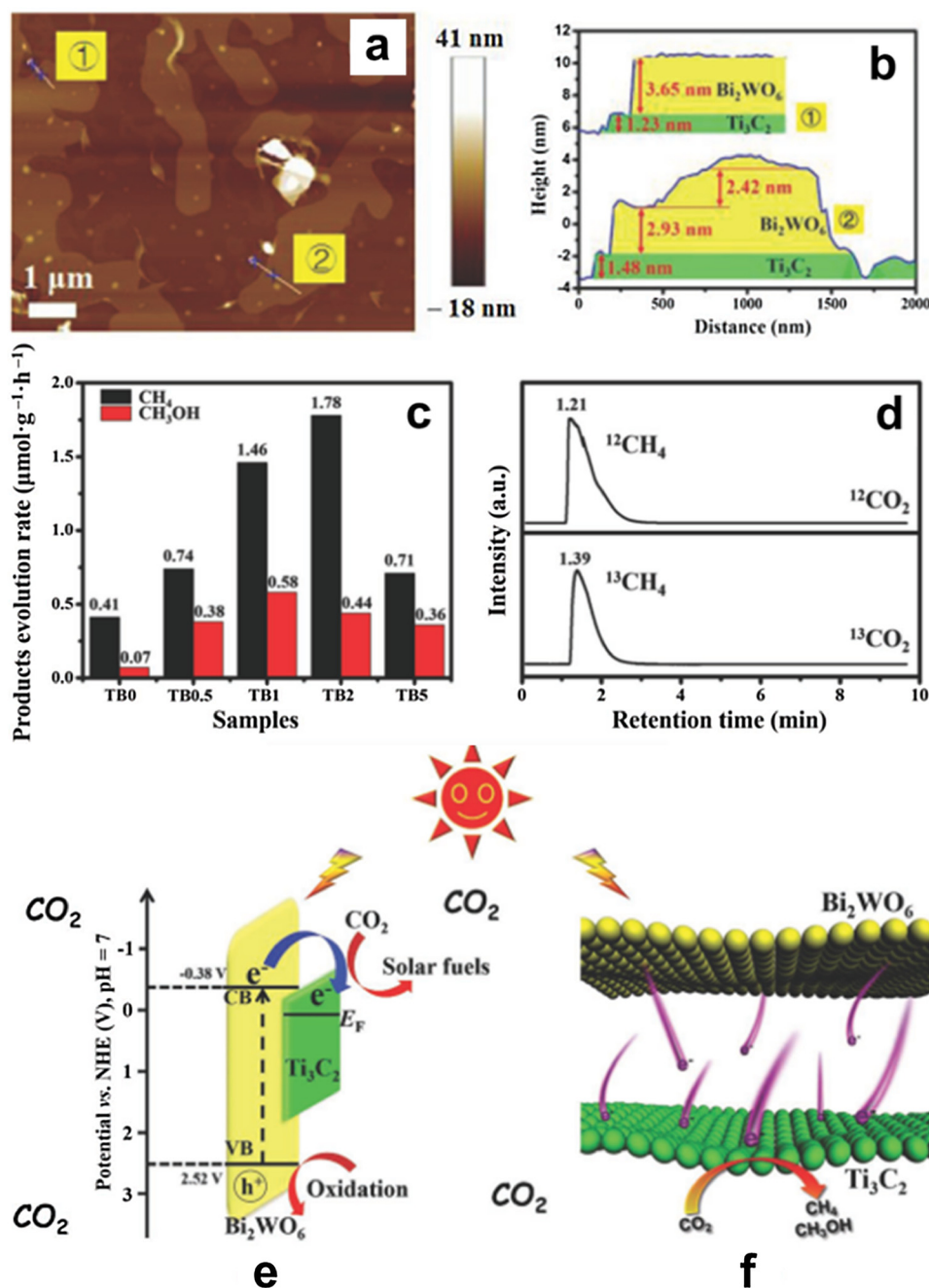
Fig. 9. (a, b) AFM images and height cutaway view of 2 wt% Ti_3C_2 modified Bi_2WO_6. (c) Photocatalytic activity of TB0 to TB5, (d) GC–MS spectra over TB2 after irradiation with different carbon sources, (e) Energy level structure diagram of Bi_2WO_6 and Ti_3C_2, (f) Photogenerated electron transfer process at the interface of the Ti_3C_2/Bi_2WO_6. reproduced with permission from ref. [101], Wiley-VCH.

separation. More effective methods should be explored to optimize this deficiency.

4.5.2. 2D-2D stacking heterojunction

Constructing 2D-2D stacking heterojunction is another efficient approach to achieve outstanding photocatalytic activity. For the ultrathin 2D materials, the lattice mismatch can be minimized due to the similar layered structures, huge contact area with intimate integration can be formed to trigger effective charge separation [108]. A typical example in CO_2 photoreduction is the construction of ultrathin Ti_3C_2/Bi_2WO_6 nanosheets (Fig. 9) [101]. This structure offers the short transport distance of charges and a large interfacial contact area, ensuring outstanding bulk-to-surface and interfacial charge transfer performances. The optimized sample shows a 4.6 times total yield of CH_4

(1.78 $\mu mol\, g^{-1}\, h^{-1}$) and CH_3OH (0.44 $\mu mol\, g^{-1}\, h^{-1}$) compared with Bi_2WO_6 nanosheets. This type of building can effective improve the accessible area around the planar interface of the 2D and 2D layers and reduce the barriers for electron transfer between two components. More effective systems are desired to be constructed with this 2D/2D configurations to further boost the CO_2 reduction performance.

4.5.3. Z-scheme system

Apart from above mentioned heterojunction types, create Z-scheme system to boost the photocatalytic activity is a hot strategy in recent years. This structure can improve the light harvesting, enable spatially separated reductive and oxidative active sites, and effective preserve the strong redox ability of each components [109,110]. For example, Yu et al. developed g-C_3N_4/SnS_2 heterojunction by modification SnS_2
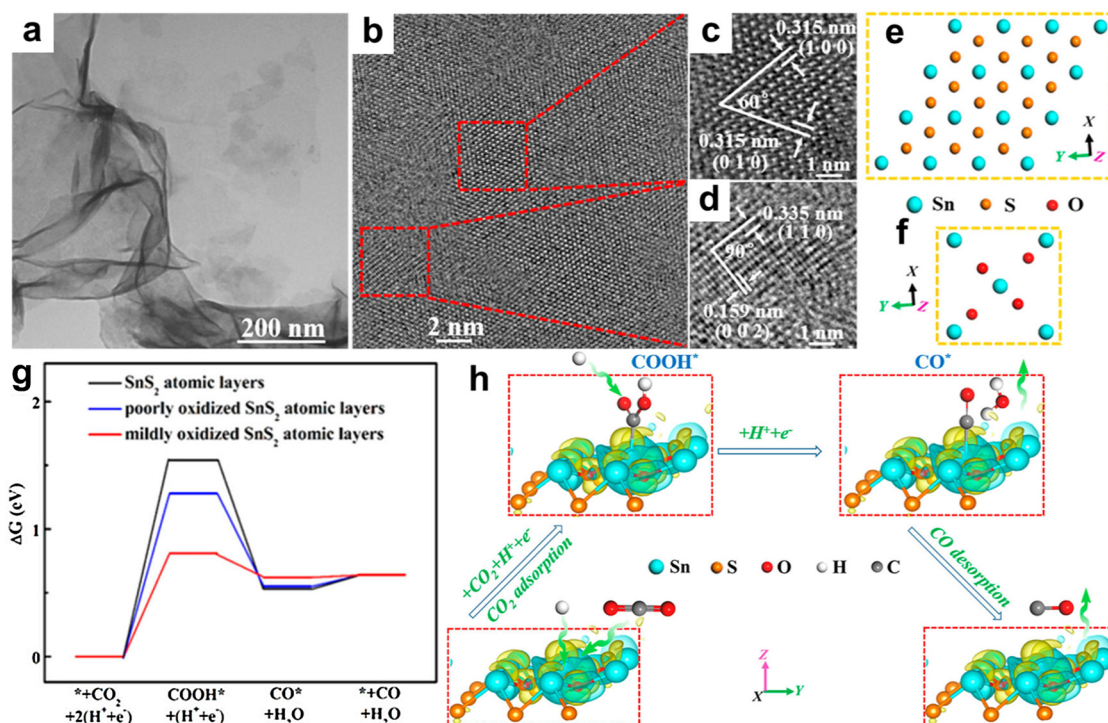
Fig. 10. (a) TEM image, (b) HRTEM image and (c, d) the corresponding enlarged HRTEM images, as well as (e, f) the related schematic atomic models. (g) Free energy diagrams of CO_2 photoreduction to CO for SnS_2 atomic layers with different oxidized degree. (h) Schematic representation of CO_2 photoreduction mechanism on the mildly oxidized SnS_2 atomic layers. reproduced with permission from ref. [43], American Chemical Society.

quantum dots onto the surface of g-C_3N_4 [107]. On the basis of experiment and calculation results, the electrons will migrate from g-C_3N_4 to SnS_2, endows the formation of interfacial internal electric fields. Under irradiation, the Z-scheme charge transfers with the electrons in SnS_2 combining with the holes in g-C_3N_4, ensure the sufficient utilization of photogenerated electrons in g-C_3N_4. Finally, effective CO_2 photoreduction occurs to yield more CH_3OH and CH_4 than single ones.

4.5.4. In-plane heterojunction

Building unique in-plane heterojunction in ultrathin structures may be another appealing strategy to tune the CO_2 photoreduction behavior [43]. Through tuning the ratio of ethylene glycol to deionized water, SnS_2 atomic layers with diverse oxidation degrees can be achieved (Fig. 10). The HRTEM images clearly prove the existence of two different structural domains in atomic layer plane, corresponding to hexagonal SnS_2 and tetragonal SnO_2, respectively. Coupled with the results of Raman spectra and XPS spectra, it prove the in-plane SnS_2/SnO_2 heterojunction have been controlled prepared. The locally oxidized domains to form SnO_2 favors the charge-carrier separation kinetics through matched energy band structures. Meanwhile, it can create electron localization on Sn atoms near the O atoms, which can stabilize the COOH* intermediates and then lower the activation energy barrier from CO_2 to COOH* intermediates over SnS_2/SnO_2 in-plane heterojunction. The optimized sample can deliver a CO production rate of 12.28 μmol g^{-1} h^{-1} under visible light, 2.6 times higher than that of SnS_2 atomic layers. Although the effective role for activity improvement, this type of in-plane heterojunction is difficult to be built due to the refined in-plane atomic structure difference with the maintain of entire ultrathin nature. Further treatment, such as ball-milling, plasma etching, on the prefabricated ultrathin materials may be a more appealing method for the controlled synthesis of in-plane heterojunction. In some condition, the inaccurate consciousness of in-plane heterojunction may be achieved only by the differentiation of HRTEM. It should be quite careful to identify the in-plane heterojunction not only from TEM or STEM images but also from sufficient spectroscopy results.

5. Conclusions and perspectives

Ultrathin structured photocatalysts with suitable energy band structure are excellent candidates towards CO_2 reduction. In this review, recent advances of ultrathin structured photocatalysts in the application of CO_2 reduction are summarized. We start with the basic understanding and some matters need attention in CO_2 photoreduction. Then advancements of various ultrathin structured photocatalysts towards CO_2 photoreduction classified as 1D ultrathin structure, 2D ultrathin structure, and 3D architectures assembled with ultrathin structures are presented. The various strategies to further tune the performance of CO_2 reduction are discussed via taming the surface coordination structure, electronic structure, carrier concentration and charge separation, so as to acquire the excellent activity, selectivity and stability.

Despite several recent advancement achieved, the related development in this area is still at an infant moment. Many opportunities are available and challenges need to be faced and addressed. Firstly, the production of diverse carbon-based fuels require different reduction potentials over photocatalysts. Since the quantum confinement effect in ultrathin materials will effective tune the energy band structures, it is desirable to control proper thickness of ultrathin materials to acquire appropriate reduction potential, so as to selective generate specific carbon-based fuels. Moreover, the strategies to tune the oxidation half reaction in water splitting for O_2 generation can also be used for CO_2 reduction since the H_2O is also ideal proton source in CO_2 photoreduction.

Secondly, there is conflicting accounts on whether the ultrathin structures are more or less stable than the bulk counterparts. The structural changes of ultrathin materials will easily happen during the reaction process, such as elastic strain. The existed strain in the structural-tuned ultrathin materials will vary electronic structure and surface nature, which has been demonstrated to be able to tailor the activity. It need further exploration to determine whether the stability is also been affected or improved. At the same time, the standardized

protocols to fairly evaluate the CO_2 photoreduction performance should be updated by considering the extraordinary high surface areas.

Thirdly, up to now, there are only small number of studies to explore the actual source of carbon-based products. Isotope labeling experiments by using $^{13}CO_2$ and $H_2^{18}O$ should be more employed to determine the authentic origin of carbon and oxygen, especially for the carbon-based ultrathin materials. It is desirable to determine whether the stoichiometric ratio of redox products can be achieved to realize CO_2 reduction.

Fourthly, the dominant reported reduction products over ultrathin materials are C_1 derivatives, especially CH_4 and CO, while multi-carbon products are rarely reported. Most studies detect only a few species of products, and more species need to be detected at the same time. Benefiting from impressive energy densities of multi-carbon hydrocarbons, such as C_2 ethylene (C_2H_4) and ethanol (C_2H_5OH), the higher economic value per unit mass can be achieved relative to C_1 counterparts. In next step, it is desirable to develop more efficient ultrathin materials for multi-carbon products generation.

Fifthly, during the CO_2 photoreduction process, the in situ FT-IR spectra is the usually used technique to explore the activation and conversion process of CO_2. More advanced in situ technique such as aberration-corrected STEM, XAFS, ultrafast spectroscopy, need to be employed to explore the material's structural changes and mode of action with CO_2 molecules, so as to deeply insight the relationship between structures with reduction performances. The more veritable theoretical studies regarding excited state need to be performed to assist experiments so as to reveal conversion process of CO_2 to products.

Acknowledgements

References

[1] D. Voiry, H.S. Shin, K.P. Loh, M. Chhowalla, Nat. Rev. Chem. 2 (2018) 0105.
[2] L.J. Liu, Y.Q. Jiang, H.L. Zhao, J.T. Chen, J.L. Cheng, K. Yang, Y. Li, ACS Catal. 6 (2016) 1097–1108.
[3] S. Sorcar, Y.J. Hwang, C.A. Grimes, S. In, Mater. Today 20 (2017) 507–515.
[4] C.T. Dinh, T. Burdyny, M.G. Kibria, A. Seifitokaldani, C.M. Gabardo, F.P.G. de Arquer, A. Kiani, J.P. Edwards, P.D. Luna, O.S. Bushuyev, C.Q. Zou, R. Quintero-Bermudez, Y.J. Pang, D. Sinton, E.H. Sargent, Science 360 (2018) 783–787.
[5] C.Y. Dong, C. Lian, S.C. Hu, Z.S. Deng, J.Q. Gong, M.D. Li, H.L. Liu, M.Y. Xing, J.L. Zhang, Nat. Commun. 9 (2018) 1252.
[6] Y. Wang, Z.Z. Zhang, L.N. Zhang, Z.B. Luo, J.N. Shen, H.X. Lin, J.L. Long, J.C.S. Wu, X.Z. Fu, X.X. Wang, C. Li, J. Am. Chem. Soc. 140 (2018) 14595–14598.
[7] J. Di, J.X. Xia, H.M. Li, Z. Liu, Nano Energy 35 (2017) 79–91.
[8] J. Di, C. Yan, A.D. Handoko, Z.W. Seh, H.M. Li, Z. Liu, Mater. Today 21 (2018) 749–770.
[9] J. Di, J.X. Xia, M.F. Chisholm, J. Zhong, C. Chen, X.Z. Cao, F. Dong, Z. Chi, H.L. Chen, Y.X. Weng, J. Xiong, S.Z. Yang, H.M. Li, Z. Liu, S. Dai, Adv. Mater. 31 (2019) 1807576.
[10] Z.Y. Sun, N. Talreja, H.C. Tao, J. Texter, M. Muhler, J. Strunk, J.F. Chen, Angew. Chem. Int. Ed. 57 (2018) 7610–7627.
[11] Y.X. Pan, Y. You, S. Xin, Y.T. Li, G.T. Fu, Z.M. Cui, Y.L. Men, F.F. Cao, S.H. Yu, J.B. Goodenough, J. Am. Chem. Soc. 139 (2017) 4123–4129.
[12] P. Li, Y. Zhou, Z.Y. Zhao, Q.F. Xu, X.Y. Wang, M. Xiao, Z.G. Zou, J. Am. Chem. Soc. 137 (2015) 9547–9550.
[13] P.J. Yang, R.R. Wang, M. Zhou, X.C. Wang, Angew. Chem. Int. Ed. 57 (2018) 8674–8677.
[14] P.J. Yang, H.Y. Zhuzhang, R.R. Wang, W. Lin, X.C. Wang, Angew. Chem. Int. Ed. 58 (2019) 1134–1137.
[15] H.J. Yu, J.Y. Li, Y.H. Zhang, S.Q. Yang, K.L. Han, F. Dong, T.Y. Ma, H.W. Huang, Angew. Chem. Int. Ed. 58 (2019) 3880–3884, https://doi.org/10.1002/anie.201813967.
[16] Y.F. Zhao, G.I.N. Waterhouse, G.B. Chen, X.Y. Xiong, L.Z. Wu, C.H. Tung, T.R. Zhang, Chem. Soc. Rev. 48 (2019) 1972–2010, https://doi.org/10.1039/c8cs00607e.
[17] B. Han, X.W. Ou, Z.Q. Deng, Y. Song, C. Tian, H. Deng, Y.J. Xu, Z. Lin, Angew. Chem. Int. Ed. 57 (2018) 16811–16815.
[18] N. Zhang, A. Jalil, D.X. Wu, S.M. Chen, Y.F. Liu, C. Gao, W. Ye, Z.M. Qi, H.X. Ju, C.M. Wang, X.J. Wu, L. Song, J.F. Zhu, Y.J. Xiong, J. Am. Chem. Soc. 140 (2018)

[19] Y.F. Sun, S. Gao, F.C. Lei, Y. Xie, Chem. Soc. Rev. 44 (2015) 623–636.
[20] L. Zhang, Z.J. Zhao, T. Wang, J.L. Gong, Chem. Soc. Rev. 47 (2018) 5423–5443.
[21] X.X. Chang, T. Wang, J.L. Gong, Energy Environ. Sci. 9 (2016) 2177–2196.
[22] N. Zhang, R. Long, C. Gao, Y.J. Xiong, Sci. China Mater. 61 (2018) 771–805.
[23] G. Liu, C. Zhen, Y.Y. Kang, L.Z. Wang, H.M. Cheng, Chem. Soc. Rev. 47 (2018) 6410–6444.
[24] Y. Ma, X.L. Wang, Y.S. Jia, X.B. Chen, H.X. Han, C. Li, Chem. Rev. 114 (2014) 9987–10043.
[25] B.Y. Wang, W. Chen, Y.F. Song, G.H. Li, W. Wei, J.H. Fang, Y.H. Sun, Catal. Today 311 (2018) 23–39.
[26] P.V. Kamat, S. Jin, ACS Energy Lett. 3 (2018) 622–623.
[27] M. Marszewski, S.W. Cao, J.G. Yu, M. Jaroniec, Mater. Horiz. 2 (2015) 261–278.
[28] Q. Liu, Y. Zhou, J.H. Kou, X.Y. Chen, Z.P. Tian, J. Gao, S.C. Yan, Z.G. Zou, J. Am. Chem. Soc. 132 (2010) 14385–14387.
[29] G.C. Xi, S.X. Ouyang, P. Li, J.H. Ye, Q. Ma, N. Su, H. Bai, C. Wang, Angew. Chem. Int. Ed. 51 (2012) 2395–2399.
[30] J. Di, C. Zhu, M.X. Ji, M.L. Duan, R. Long, C. Yan, K.Z. Gu, J. Xiong, Y.B. She, J.X. Xia, H.M. Li, Z. Liu, Angew. Chem. Int. Ed. 57 (2018) 14847–14851.
[31] S.K. Parayil, A. Razzaq, S.M. Park, H.R. Kim, C.A. Grimes, S. In, Appl. Catal. A 498 (2015) 205–213.
[32] C.Y. Huang, R.T. Guo, W.G. Pan, J.Y. Tang, W.G. Zhou, X.Y. Liu, H. Qin, P.Y. Jia, Appl. Surf. Sci. 464 (2019) 534–543.
[33] H.P. Wang, L. Zhang, K.F. Wang, X. Sun, W.Z. Wang, Appl. Catal. B 243 (2019) 771–779.
[34] S.C. Feng, X.Y. Chen, Y. Zhou, W.G. Tu, P. Li, H.J. Li, Z.G. Zou, Nanoscale 6 (2014) 1896–1900.
[35] Q. Liu, Y. Zhou, Y. Ma, Z.G. Zou, RSC Adv. 2 (2012) 3247–3250.
[36] J.R. Jin, T. He, Appl. Surf. Sci. 394 (2017) 364–370.
[37] S.M. Sun, M. Watanabe, J. Wu, Q. An, T. Ishihara, J. Am. Chem. Soc. 140 (2018) 6474–6482.
[38] S. Qamar, F.C. Lei, L. Liang, S. Gao, K.T. Liu, Y.F. Sun, W.X. Ni, Y. Xie, Nano Energy 26 (2016) 692–698.
[39] X.Y. Chen, Y. Zhou, Q. Liu, Z.D. Li, J.G. Liu, Z.G. Zou, ACS Appl. Mater. Interfaces 4 (2012) 3372–3377.
[40] L. Liang, X.D. Li, Y.F. Sun, Y.L. Tan, X.C. Jiao, H.X. Ju, Z.M. Qi, J.F. Zhu, Y. Xie, Joule 2 (2018) 1–13.
[41] W.Y. Chen, B. Han, C. Tian, X.M. Liu, S.J. Liang, H. Deng, Z. Lin, Appl. Catal. B 244 (2019) 996–1003.
[42] X.D. Li, L. Liang, Y.F. Sun, J.Q. Xu, X.C. Jiao, X.L. Xu, H.X. Ju, Y. Pan, J.F. Zhu, Y. Xie, J. Am. Chem. Soc. 141 (2019) 423–430.
[43] X.C. Jiao, X.D. Li, X.Y. Jin, Y.F. Sun, J.Q. Xu, L. Liang, H.X. Ju, J.F. Zhu, Y. Pan, W.S. Yan, Y. Lin, Y. Xie, J. Am. Chem. Soc. 139 (2017) 18044–18051.
[44] B. Pan, Y. Wu, J.N. Qin, C.Y. Wang, Catal. Today (2019), https://doi.org/10.1016/j.cattod.2018.11.017.
[45] X.C. Jiao, Z.W. Chen, X.D. Li, Y.F. Sun, S. Gao, W.S. Yan, C.M. Wang, Q. Zhang, Y. Lin, Y. Luo, Y. Xie, J. Am. Chem. Soc. 139 (2017) 7586–7594.
[46] S.J. Xie, Y. Wang, Q.H. Zhang, W.P. Deng, Y. Wang, Chem. Commun. 51 (2015) 3430–3433.
[47] Y.F. Zhao, G.B. Chen, T. Bian, C. Zhou, G.I.N. Waterhouse, L.Z. Wu, C.H. Tung, L.J. Smith, D. O'Hare, T.R. Zhang, Adv. Mater. 27 (2015) 7824–7831.
[48] H.J. Yu, H.W. Huang, K. Xu, W.C. Hao, Y.X. Guo, S.B. Wang, X.L. Shen, S.F. Pan, Y.H. Zhang, ACS Sustain. Chem. Eng. 5 (2017) 10499–10508.
[49] X.Y. Kong, B.J. Ng, K.H. Tan, X.F. Chen, H.T. Wang, A.R. Mohamed, S.P. Chai, Catal. Today 314 (2018) 20–27.
[50] L.Q. Ye, X.L. Jin, C. Liu, C.H. Ding, H.Q. Xie, K.H. Chu, P.K. Wong, Appl. Catal. B 187 (2016) 281–290.
[51] Y. Bai, P. Yang, L. Wang, B. Yang, H.Q. Xie, Y. Zhou, L.Q. Ye, Chem. Eng. J. 360 (2019) 473–482.
[52] L.Q. Ye, X.L. Jin, X.X. Ji, C. Liu, Y.R. Su, H.Q. Xie, C. Liu, Chem. Eng. J. 291 (2016) 39–46.
[53] L. Liang, F.C. Lei, S. Gao, Y.F. Sun, X.C. Jiao, J. Wu, S. Qamar, Y. Xie, Angew. Chem. Int. Ed. 54 (2015) 13971–13974.
[54] S. Gao, B.C. Gu, X.C. Jiao, Y.F. Sun, X.L. Zu, F. Yang, W.G. Zhu, C.M. Wang, Z.M. Feng, B.J. Ye, Y. Xie, J. Am. Chem. Soc. 139 (2017) 3438–3445.
[55] L. Ye, Y. Gao, S.Y. Cao, H. Chen, Y.N. Yao, J.G. Hou, L.C. Sun, Appl. Catal. B 227 (2018) 54–60.
[56] S.Y. Zhu, S.J. Liang, Y. Wang, X.Y. Zhang, F.Y. Li, H.X. Lin, Z.Z. Zhang, X.X. Wang, Appl. Catal. B 187 (2016) 11–18.
[57] S.B. Wang, B.Y. Guan, Y. Lu, X.W. Lou, J. Am. Chem. Soc. 139 (2017) 17305–17308.
[58] S.B. Wang, B.Y. Guan, X.W. Lou, J. Am. Chem. Soc. 140 (2018) 5037–5040.
[59] S.B. Wang, B.Y. Guan, X.W. Lou, Energy Environ. Sci. 11 (2018) 306–310.
[60] P.F. Xia, B.C. Zhu, J.G. Yu, S.W. Cao, M. Jaroniec, J. Mater. Chem. A 5 (2017) 3230–3238.
[61] Q. Liu, D. Wu, Y. Zhou, H.B. Su, R. Wang, C.F. Zhang, S.C. Yan, M. Xiao, Z.G. Zou, ACS Appl. Mater. Interfaces 6 (2014) 2356–2361.
[62] C.J. Huang, C. Chen, M.W. Zhang, L.H. Lin, X.X. Ye, S. Lin, M. Antonietti, X.C. Wang, Nat. Commun. 6 (2015) 7698.
[63] K.F. Wang, L. Zhang, Y. Su, S.M. Sun, Q.Q. Wang, H.P. Wang, W.Z. Wang, Catal. Sci. Technol. 8 (2018) 3115–3122.
[64] K.T. Liu, X.D. Li, L. Liang, J. Wu, X.C. Jiao, J.Q. Xu, Y.F. Sun, Y. Xie, Nano Res. 11 (2018) 2897–2908.
[65] J. Xiong, J. Di, J.X. Xia, W.S. Zhu, H.M. Li, Adv. Funct. Mater. 28 (2018) 1801983.
[66] J. Di, X.X. Zhao, C. Lian, M.X. Ji, J.X. Xia, J. Xiong, W. Zhou, X.Z. Cao, Y.B. She, H.L. Liu, K.P. Loh, S.J. Pennycook, H.M. Li, Z. Liu, Nano Energy 61 (2019) 54–59.

[67] Y.Q. Guo, B.H. Dai, J. Peng, C.Z. Wu, Y. Xie, J. Am. Chem. Soc. 141 (2019) 723–732.

[68] J. Wu, X.D. Li, W. Shi, P.Q. Ling, Y.F. Sun, X.C. Jiao, S. Gao, L. Liang, J.Q. Xu, W.S. Yan, C.M. Wang, Y. Xie, Angew. Chem. Int. Ed. 57 (2018) 8719–8723.

[69] J.G. Hou, S.Y. Cao, Y.Z. Wu, F. Liang, Y.F. Sun, Z.S. Lin, L.C. Sun, Nano Energy 32 (2017) 359–366.

[70] T. Ohno, T. Higo, N. Murakami, H. Saito, Q. Zhang, Y. Yang, T. Tsubota, Appl. Catal. B 152 (2014) 309–316.

[71] J. Di, J.X. Xia, H.M. Li, S.J. Guo, S. Dai, Nano Energy 41 (2017) 172–192.

[72] C. Gao, Q.Q. Meng, K. Zhao, H.J. Yin, D.W. Wang, J. Guo, S.L. Zhao, L. Chang, M. He, Q.X. Li, H.J. Zhao, X.J. Huang, Y. Gao, Z.Y. Tang, Adv. Mater. 28 (2016) 6485–6490.

[73] J.G. Yu, J.X. Low, W. Xiao, P. Zhou, M. Jaroniec, J. Am. Chem. Soc. 136 (2014) 8839–8842.

[74] J.R. Ran, M. Jaroniec, S.Z. Qiao, Adv. Mater. 30 (2018) 1704649.

[75] Y.N. Liu, C.L. Miao, P.F. Yang, Y.F. He, J.T. Feng, D.Q. Li, Appl. Catal. B 244 (2019) 919–930.

[76] Q.Q. Wang, K.F. Wang, L. Zhang, H.P. Wang, W.Z. Wang, Appl. Surf. Sci. 470 (2019) 832–839.

[77] Q.Q. Lang, W.L. Hu, P.H. Zhou, T.L. Huang, S.X. Zhong, L.N. Yang, J.R. Chen, S. Bai, Nanotechnology 28 (2017) 484003.

[78] Y.Z. Zhu, Z.X. Xu, W.Y. Jiang, S.X. Zhong, L.H. Zhao, S. Bai, J. Mater. Chem. A 5 (2017) 2619–2628.

[79] Y.Z. Zhu, C. Gao, S. Bai, S.M. Chen, R. Long, L. Song, Z.Q. Li, Y.J. Xiong, Nano Res. 10 (2017) 3396–3406.

[80] F. Ye, F. Wang, C.C. Meng, L.J. Bai, J.Y. Li, P.X. Xing, B.T. Teng, L.H. Zhao, S. Bai, Appl. Catal. B 230 (2018) 145–153.

[81] Y.Z. Zhu, Z.X. Xu, Q.Q. Lang, W.Y. Jiang, Q.Q. Yin, S.X. Zhong, S. Bai, Appl. Catal. B 206 (2017) 282–292.

[82] G. Yin, M. Nishikawa, Y. Nosaka, N. Srinivasan, D. Atarashi, E. Sakai, M. Miyauchi, ACS Nano 9 (2015) 2111–2119.

[83] G.D. Shi, L. Yang, Z.W. Liu, X. Chen, J.Q. Zhou, Y. Yu, Appl. Surf. Sci. 427 (2018) 1165–1173.

[84] X.G. Li, W.T. Bi, Z. Wang, W.G. Zhu, W.S. Chu, C.Z. Wu, Y. Xie, Nano Res. 11 (2018) 3362–3370.

[85] R. Long, Y. Li, Y. Liu, S.M. Chen, X.S. Zheng, C. Gao, C.H. He, N.S. Chen, Z.M. Qi, L. Song, J. Jiang, J.F. Zhu, Y.J. Xiong, J. Am. Chem. Soc. 139 (2017) 4486–4492.

[86] L.H. Zhao, F. Ye, D.M. Wang, X.T. Cai, C.C. Meng, H.S. Xie, J.L. Zhang, S. Bai, ChemSusChem 11 (2018) 3524–3533.

[87] X.T. Cai, A. Wang, J.W. Wang, R.X. Wang, S.X. Zhong, Y.L. Zhao, L.J. Wu, J.R. Chen, S. Bai, J. Mater. Chem. A 6 (2018) 17444–17456.

[88] Q.Q. Lang, Y.J. Yang, Y.Z. Zhu, W.L. Hu, W.Y. Jiang, S.X. Zhong, P.J. Gong, B.T. Teng, L.H. Zhao, S. Bai, J. Mater. Chem. A 5 (2017) 6686–6694.

[89] X.Y. Kong, W.L. Tan, B.J. Ng, S.P. Chai, A.R. Mohamed, Nano Res. 10 (2017) 1720–1731.

[90] C. Han, Y.P. Lei, B. Wang, Y.D. Wang, ChemSusChem 11 (2018) 4237–4245.

[91] J. Di, C. Chen, S.Z. Yang, S.M. Chen, M.L. Duan, J. Xiong, C. Zhu, R. Long, W. Hao, Z. Chi, H.L. Chen, Y.X. Weng, J.X. Xia, L. Song, S.Z. Li, H.M. Li, Z. Liu, Nat. Commun. (2019), https://doi.org/10.1038/s41467-019-10392-w.

[92] Y.J. Cao, S. Chen, Q.Q. Luo, H. Yan, Y. Lin, W. Liu, L.L. Cao, J.L. Lu, J.L. Yang, T. Yao, S.Q. Wei, Angew. Chem. Int. Ed. 56 (2017) 12191–12196.

[93] Q.J. Xiang, B. Cheng, J.G. Yu, Angew. Chem. Int. Ed. 54 (2015) 11350–11366.

[94] H.T. Li, X.Y. Zhang, D.R. MacFarlane, Adv. Energy Mater. 5 (2015) 1401077.

[95] H.J. Li, Y. Zhou, W.G. Tu, J.H. Ye, Z.G. Zou, Adv. Funct. Mater. 25 (2015) 998–1013.

[96] L. Shi, T. Wang, H.B. Zhang, K. Chang, J.H. Ye, Adv. Funct. Mater. 25 (2015) 5360–5367.

[97] J. Ren, S.X. Ouyang, H. Xu, X.G. Meng, T. Wang, D.F. Wang, J.H. Ye, Adv. Energy Mater. 7 (2017) 1601657.

[98] M. Zhou, S.B. Wang, P.J. Yang, C.J. Huang, X.C. Wang, ACS Catal. 8 (2018) 4928–4936.

[99] G.L. Xu, H.B. Zhang, J. Wei, H.X. Zhang, X. Wu, Y. Li, C.S. Li, J. Zhang, J.H. Ye, ACS Nano 12 (2018) 5333–5340.

[100] A. Crakea, K.C. Christoforidisa, R. Godinb, B. Mossb, A. Kafizasb, S. Zafeiratosc, J.R. Durrantb, C. Petit, Appl. Catal. B 242 (2019) 369–378.

[101] S.W. Cao, B.J. Shen, T. Tong, J.W. Fu, J.G. Yu, Adv. Funct. Mater. 28 (2018) 1800136.

[102] M. Zhou, S.B. Wang, P.J. Yang, Z.S. Luo, R.S. Yuan, A.M. Asiri, M. Wakeel, X.C. Wang, Chem. Eur. J. 24 (2018) 18529–18534.

[103] X.W. Zhu, H.Y. Ji, J.J. Yi, J.M. Yang, X.J. She, P.H. Ding, L. Li, J.J. Deng, J.C. Qian, H. Xu, H.M. Li, Ind. Eng. Chem. Res. 57 (2018) 17394–17400.

[104] J.C. Wang, H.C. Yao, Z.Y. Fan, L. Zhang, J.S. Wang, S.Q. Zang, Z.J. Li, ACS Appl.

[105] M. Wang, Q.T. Han, L. Li, L.Q. Tang, H.J. Li, Y. Zhou, Z.G. Zou, Nanotechnology 28 (2017) 274002.

[106] L. Yuan, K.Q. Lu, F. Zhang, X.Z. Fu, Y.J. Xu, Appl. Catal. B 237 (2018) 424–431.

[107] T.M. Di, B.C. Zhu, B. Cheng, J.G. Yu, J.S. Xu, J. Catal. 352 (2017) 532–541.

[108] J. Di, J. Xiong, H.M. Li, Z. Liu, Adv. Mater. 30 (2018) 1704548.

[109] T. Ohno, N. Murakami, T. Koyanagi, Y. Yang, J. CO$_2$ Util. 6 (2014) 17–25.

[110] Q.L. Xu, L.Y. Zhang, J.G. Yu, S. Wageh, A.A. Al-Ghamdi, M. Jaroniec, Mater. Today 21 (2018) 1042–1063.

Mater. Interfaces 8 (2016) 3765–3775.

Jun Xiong received her BS degree from Hainan Normal University and PhD degree from Jiangsu University in 2010 and 2015, respectively. She is a research staff at Nanyang Technological University. Her current research interests focus on the synthesis of low dimensional materials for adsorption and photo-, electrocatalytic applications.
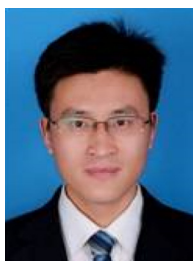
Pin Song received his Ph.D. under the supervision of Prof. Shu-Hong Yu at the Hefei University of Technology (HFUT) in 2018. He is now working as a research fellow at Nanyang Technological University in the research group of Prof. Zheng Liu. His research interests mainly focuses on the synthesis of novel two-dimensional materials and controlled synthesis of novel architectures for flexible electronic devices.

Jun Di received his BS degree in (2012) and PhD degree (2018) from Jiangsu University (with Professor Huaming Li). He is carrying on postdoctoral research at Nanyang Technological University with Professor Zheng Liu. His research interests focus on design and synthesis of 2D materials for energy conversion.

Huaming Li received his BS degree from China West Normal University in 1985 and master degree from Chinese Academy of Sciences in 1992. At present, he is a full professor at the Jiangsu University. His current research is focused on nanomaterials, ionic liquids for energy and environmental applications. He is the author and co-author of 470 original research papers published in SCI journals. The total number of citations for his work has reached about 14,000 and his H-index has arrived at 65.